

2001

Pattern Formation in Non-Newtonian Hele-Shaw Flow

P. Fast

L. Kondic

M. J. Shelley

Peter Palffy-Muhoray

Kent State University - Kent Campus, mpalffy@cpip.kent.edu

Follow this and additional works at: <https://digitalcommons.kent.edu/cpippubs>

 Part of the [Physics Commons](#)

Recommended Citation

Fast, P.; Kondic, L.; Shelley, M. J.; and Palffy-Muhoray, Peter (2001). Pattern Formation in Non-Newtonian Hele-Shaw Flow. *Physics of Fluids* 13(5), 1191-1212. doi: 10.1063/1.1359417 Retrieved from <https://digitalcommons.kent.edu/cpippubs/239>

This Article is brought to you for free and open access by the Department of Chemical Physics at Digital Commons @ Kent State University Libraries. It has been accepted for inclusion in Chemical Physics Publications by an authorized administrator of Digital Commons @ Kent State University Libraries. For more information, please contact digitalcommons@kent.edu.

Pattern formation in non-Newtonian Hele–Shaw flow

Petri Fast^{a)}

Courant Institute of Mathematical Sciences, New York University, New York, New York 10012

L. Kondic

*Department of Mathematical Sciences and Center for Applied Mathematics and Statistics,
New Jersey Institute of Technology, Newark, New Jersey 07102*

Michael J. Shelley

Courant Institute of Mathematical Sciences, New York University, New York, New York 10012

Peter Palffy-Muhoray

Liquid Crystal Institute, Kent State University, Kent, Ohio 44242

(Received 29 December 1998; accepted 7 February 2001)

We study theoretically the Saffman–Taylor instability of an air bubble expanding into a non-Newtonian fluid in a Hele–Shaw cell, with the motivation of understanding suppression of tip-splitting and the formation of dendritic structures observed in the flow of complex fluids, such as polymeric liquids or liquid crystals. A standard visco-elastic flow model is simplified in the case of flow in a thin gap, and it is found that there is a distinguished limit where shear thinning and normal stress differences are apparent, but elastic response is negligible. This observation allows formulation of a generalized Darcy’s law, where the pressure satisfies a nonlinear elliptic boundary value problem. Numerical simulation shows that shear-thinning alone modifies considerably the pattern formation and can produce fingers whose tip-splitting is suppressed, in agreement with experimental results. These fingers grow in an oscillating fashion, shedding “side-branches” from their tips, closely resembling solidification patterns. A careful analysis of the parametric dependencies of the system provides an understanding of the conditions required to suppress tip-splitting, and an interpretation of experimental observations, such as emerging length-scales.

© 2001 American Institute of Physics. [DOI: 10.1063/1.1359417]

I. INTRODUCTION

While flows of non-Newtonian fluids are of considerable technological importance, their understanding is often obscured by their complexity. For this reason, we concentrate on a rather simple situation: fluid flow in the essentially two-dimensional setting of a Hele–Shaw cell, where the flow is described by a balance between pressure and viscous forces, and which for a Newtonian fluid is governed by Darcy’s law. Such thin-gap flows of non-Newtonian fluids are relevant to industrial processes such as injection molding¹ or display device design.² In particular, a two-phase flow in this setting is a scientifically important one, given the close analogy between the Saffman–Taylor instability of driven Newtonian fluid with quasistatic solidification (and the Mullins–Sekerka instability³), and many other physical problems, such as electrochemical deposition.⁴

To make contact with a large body of experimental and theoretical work on pattern formation in such systems, we concentrate here on the interfacial dynamics of a gas bubble expanding into fluid in a radial Hele–Shaw cell. When the fluid is Newtonian, a dense branching pattern morphology is commonly observed (see McCloud and Maher⁵ and the ref-

erences therein) as the outcome of the nonlinear development of the Saffman–Taylor instability. Such patterns are characterized by successive tip-splitting of the interface, the formation of branched structures, and the competition between them. This morphology has been observed in careful numerical simulations,⁶ and described in some of its aspects theoretically.⁷ It is also well known that flow structures reminiscent of solidification—dendritic fingers, side-branching, suppressed tip-splitting—can be produced in such Newtonian flows by imposing an anisotropy on the system, for example, by scoring lines on the plates,⁸ or by introducing a perturbation (bubble) in the fluid itself.⁹ Again, some detailed understanding of these systems has been achieved through analysis and simulation (see, for example Almgren, Dai, and Hakim¹⁰).

However, experiments performed with complex liquids such as liquid crystals,^{11,12} polymer solutions and melts,^{13,14} clays,¹⁵ and foams,¹⁶ have shown that similar structures can be induced by the bulk properties of the fluid itself. That is, the response of the fluid, which may itself be isotropic, can produce an effect akin to anisotropy. One property shared by these different liquids is that they are shear-thinning (the shear viscosity decreases with the local shear rate), and we will concentrate on this property.

As a motivating example, Figs. 1(a) and 1(b) show an experiment of the pattern formation that results from pushing

^{a)}Present address: Center for Applied Scientific Computing, Lawrence Livermore National Laboratory, P.O. Box 808, L-661, Livermore, California 94551.

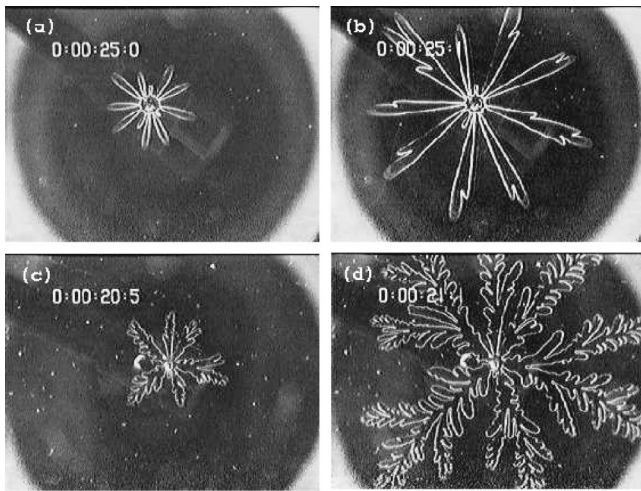


FIG. 1. Graphs (a) and (b) show the temporal development of a pattern that results from pushing air into a dilute, shear-thinning PEO solution in a Hele–Shaw cell. Graphs (c) and (d) show the resulting pattern in a cell with gap width 2.5 times smaller. The driving pressures are the same in either case. Figures courtesy of Ennis and Palfy-Muhoray, LCI, Kent State.

air into a dilute solution of PEO, a standard shear-thinning polymer (figures courtesy of R. Ennis and P. Palfy-Muhoray, LCI, Kent State). A relative lack of tip-splitting is apparent, and one sees the appearance of isolated fingers. Holding the driving pressure fixed, Figs. 1(c) and 1(d) show the effect of decreasing the gap width by 2.5 times. This decreases the non-Newtonian effect by lowering the Weissenberg number (defined as the ratio of the material relaxation time to a fluid flow time), and one observes the emergence of tip-splitting and of a more densely branched pattern. In either case, the similarity to dendritic structures is clear.

As an illustrative case, our analysis uses the Johnson–Segalman–Oldroyd (JSO) model¹⁷ for a viscoelastic fluid, though our results apply to more general differential models (Sec. II). This model considerably simplifies in the thin-gap limit $\epsilon = b/L \ll 1$, where b is the separation between the plates and L is some typical lateral dimension (Sec. II A). To the leading order in ϵ , we find that there is a distinguished limit—where the natural Weissenberg number of the flow is $O(1)$ —where shear-thinning is retained. In this limit, the viscoelastic fluid is reduced to a generalized Newtonian fluid, where elastic effects enter only through the definition of a Weissenberg number. Following our previous work,^{18,19} we obtain then a generalized Darcy’s law governing the bulk fluid flow,

$$\mathbf{u} = - \frac{\nabla_2 p}{\bar{\mu}(\text{We}^2 |\nabla_2 p|^2)}, \quad \nabla_2 \cdot \mathbf{u} = 0, \quad (1)$$

where \mathbf{u} is the gap averaged longitudinal velocity, p is the fluid pressure, We is a Weissenberg number, and $\bar{\mu}$ is a derived effective viscosity depending upon the squared pressure gradient. This yields a nonlinear, elliptic boundary value problem (BVP) for the pressure in the driven fluid (Sec. II B). Issues related to boundary conditions for this BVP are discussed in Sec. II B 1. As it appears appropriate for the

parametric regime which we study, in our simulations we use the Laplace–Young condition, as is typically used for Newtonian Hele–Shaw flows.

In recent theoretical work, Poiré and Ben Amar^{20,21} have used our prescription to study the formation of “fractures” or “cracks” in clays and associating polymer solutions.²⁰ Using a shear-thinning power-law fluid, they examined the “width selection” problem for a gas finger propagating steadily down a channel. They consider the displaced fluid to be slightly shear-thinning (in the shear-thinning exponent), and show within this asymptotic limit, the selected finger width decreases to zero (i.e., a crack) as surface tension goes to zero. Lindner, Bonn, and Meunier²² recently studied experimentally the propagation of a finger into a shear-thinning liquid. Also using Eq. (1) for a power-law fluid, they find excellent agreement with their experimental data.

In Sec. III, we examine the linear stability of a circular, expanding gas bubble, where the driven fluid is governed by the generalized Darcy’s law. We consider first a weakly non-Newtonian model where, in the limit of a small Weissenberg number, the nonlinear boundary value problem for the pressure is simplified to a linear one, and the linear stability problem can be solved exactly. This suggests that shear-thinning can modify the Saffman–Taylor instability to give increased length-scale selection. We expand on this further by solving numerically the linear stability problem for a strongly shear-thinning fluid. In Sec. IV we perform fully nonlinear, time dependent simulations of a bubble growing into a strongly shear-thinning fluid. These simulations show that shear-thinning influences considerably the evolution of the interface, and in agreement with experiments with complex fluids, can lead to the formation of fingers which do not split, and that grow in an oscillating fashion. They can resemble closely the dendritic structures observed in solidification. We also analyze the dependence of the interface morphology on nondimensional parameters, which allows a comparison with and interpretation of available experimental results (Sec. V). Finally, we also explore some different viscosity models and discuss computed and experimentally observed length-scales. In the Appendix, we discuss the mathematical aspects of solving for the effective viscosity $\bar{\mu}$, and the relation to the solvability of the nonlinear BVP (1).

II. EQUATIONS OF MOTION

First, for thin gap (Hele–Shaw) flow we show how a “typical” visco-elastic flow model reduces asymptotically to the non-Newtonian Darcy’s law (1). We then discuss boundary conditions at the gas/fluid interface. At the end of the section, we formulate the flow problem as the dynamics of the gas/fluid interface, whose velocity is found by solving a nonlinear BVP over the fluid domain encompassed by the interface.

A model for the motion of an incompressible, isothermal, viscoelastic fluid is given by

$$\rho \frac{D\mathbf{v}}{Dt} = \nabla \cdot \boldsymbol{\tau}, \quad (2)$$

$$\nabla \cdot \mathbf{v} = 0, \quad (3)$$

together with a constitutive relation for the stress tensor $\boldsymbol{\tau}$. Here $\mathbf{v}=(u,v,w)$ is the velocity field, $D/Dt=\partial_t+\mathbf{v}\cdot\nabla$ is the material derivative, and ρ is the (constant) density. The velocity gradient is $(\nabla\mathbf{v})_{ij}=\partial_jv_i$, and $\mathcal{D}=(\nabla\mathbf{v}+\nabla\mathbf{v}^T)/2$ is the rate-of-strain tensor.

When studying a particular flow problem, it is important to pick a constitutive relation that reproduces the experimental observations for the relevant rheometric flows. In the case of Hele–Shaw flow, we show how to derive the generalized Darcy’s law (1) for a broad class of differential models. We illustrate this within the context of the Johnson–Segalman–Oldroyd (JSO) model^{17,23} with a single relaxation time. This is perhaps the simplest viscoelastic model that captures normal stress differences and shear-thinning of the viscosity. The JSO equations are

$$\boldsymbol{\tau}=-p\mathcal{I}+2\mu_s\mathcal{D}+\boldsymbol{\sigma}, \tag{4}$$

$$\boldsymbol{\sigma}+\lambda\frac{D_a\boldsymbol{\sigma}}{Dt}=2\mu_p\mathcal{D}, \tag{5}$$

where p is the pressure, $\boldsymbol{\sigma}$ is the extra stress tensor, λ is the relaxation time, and μ_s and μ_p are the solvent and polymer viscosities.

The Gordon–Schowalter (GS) convected derivative,²⁴

$$\frac{D_a\boldsymbol{\sigma}}{Dt}=\frac{D\boldsymbol{\sigma}}{Dt}-\{\nabla\mathbf{v}\boldsymbol{\sigma}+\boldsymbol{\sigma}\nabla\mathbf{v}^T\}+(1-a)\{\mathcal{D}\boldsymbol{\sigma}+\boldsymbol{\sigma}\mathcal{D}\}, \tag{6}$$

in JSO models the nonaffine motion of polymer chains. They are not locked into a rubber network, which deforms with the flow, but rather the chains are allowed to slip past the continuum. For $a=1$ the motion is affine, and JSO reduces to the Oldroyd-B model, which for $\mu_s=0$ is the same as the upper-convected Maxwell model. Decreasing a increases the slippage, and softens the response of the material by increasing shear-thinning in shear flows, and reducing strain hardening in extensional flows. [The slip-parameter a should be restricted to $0.2 < a < 0.89$ for consistency with experiments²⁵ using dilute solutions of a variety of commercial polymers. The ratio of the second normal stress difference to the first, equal to $-(1-a)/2$ for JSO, was found to lie between -0.40 and -0.055 , and to be independent of the shear-rate.] The GS-derivative reduces to the corotational derivative for $a=0$, and to the lower-convected derivative for $a=-1$.

A. A Hele–Shaw scaling of JSO

In this section, we use the small aspect ratio $\varepsilon=b/L$ of the gap width b to the lateral length-scale L to derive the generalized Darcy’s law (1). This is done by choosing the pressure $p\propto\varepsilon^{-1}$, which makes shear-thinning a dominant effect and leaves the elastic response a higher order correction.

1. One-dimensional steady shear flow

We expect a non-Newtonian Hele–Shaw flow to behave locally like a one-dimensional steady shear-flow in the direction of the pressure gradient. To understand the scaling of the full equations (2)–(4), we consider a steady, one-dimensional shear flow $\mathbf{v}(z)=(u(z),0,0)$. Partial derivatives

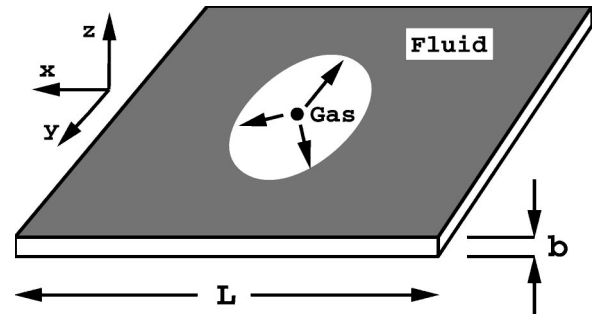


FIG. 2. Hele–Shaw cell.

are denoted by a subscript and the components of a tensor by a superscript, e.g., the xx -component of $\boldsymbol{\sigma}$ is σ^{xx} .

The extra stress tensor $\boldsymbol{\sigma}$ can be solved explicitly from (5) without approximation.²⁶ The extra stress components are given by

$$\sigma^{xz}=\frac{\mu_p}{1+(1-a^2)\lambda^2u_z^2}u_z, \quad \sigma^{xx}=(1+a)\lambda u_z\sigma^{xz}, \tag{7}$$

$$\sigma^{yy}=0, \quad \sigma^{zz}=-\lambda(1-a)u_z\sigma^{xz}. \tag{8}$$

The steady momentum equations (2) are then

$$p_x=\frac{\partial}{\partial z}(\mu(u_z^2)u_z), \tag{9}$$

$$p_y=0, \tag{10}$$

$$p_z=-\frac{\partial}{\partial z}((1-a)\lambda\mu(u_z)u_z^2), \tag{11}$$

where the shear-rate dependent viscosity μ is defined by

$$\mu(u_z^2)=\mu_0\frac{1+\alpha(1-a^2)\lambda^2u_z^2}{1+(1-a^2)\lambda^2u_z^2}, \tag{12}$$

and $\mu_0=\mu_s+\mu_p$ is the total, or zero shear-rate, viscosity.

The ‘‘shear-thinning parameter’’ $\alpha=\mu_s/\mu_0$ determines the behavior of the viscosity function: $\alpha=1$ yields a Newtonian fluid with a constant viscosity, and $\alpha < 1$ yields a viscosity that increases with decreasing shear-rate, i.e., the viscosity is shear-thinning. The constraint $\alpha > 1/9$ is necessary for the stress–strain relation to be invertible (see Sec. II B).

We now nondimensionalize Eq. (9), and study the effect of different scalings of the pressure. For a given fluid, the experimentally adjustable quantities are the driving (gauge) pressure δP and the plate separation b . The lateral length scale L is given by some typical dimension in the horizontal direction, such as the size of the cell or an initial bubble size, which is large in comparison to b , so that $\varepsilon=b/L\ll 1$ (Fig. 2). The characteristic lateral velocity U will also depend on the driving pressure. We scale $z\sim b$, $x\sim L$, $p\sim\delta P$ and $u\sim U$, and write Eq. (9) nondimensionally as

$$\frac{\delta P}{L}\frac{\partial p}{\partial x}=\frac{\mu_0U}{b^2}\frac{\partial}{\partial z}\left(\frac{1+\alpha(1-a^2)We'^2u_z^2}{1+(1-a^2)We'^2u_z^2}u_z\right). \tag{13}$$

Here $We'=\lambda U/b$ is a Weissenberg number.²⁶

We now choose the pressure scaling. Balancing pressure and viscous forces gives $U = \varepsilon^2 \delta PL / \mu_0$. If δP is independent of ε , then $We' \propto \varepsilon$, and (13) reduces to the Newtonian case with viscosity $\mu_0 = \mu_s + \mu_p$. If $\delta P \propto \varepsilon^{-2}$, then $We' \propto \varepsilon^{-1}$, the shear-viscosity will be constant, and elastic effects would become important in an unsteady flow.

The choice that makes shear-thinning apparent is $\delta P \propto \varepsilon^{-1}$. Then $U \propto \varepsilon$, $We' \propto 1$, and (13) retains its shear-thinning character in the leading order as $\varepsilon \rightarrow 0$. This is a distinguished limit, as a specific scaling of the independent and dependent variables is required to retain some desired quality, in our case the shear-rate dependency of the viscosity.

2. Nondimensional form of JSO for Hele–Shaw flow

In this section, the full equations of motion (2)–(5) are nondimensionalized. The one-dimensional shear flow solution suggests the following scaling (the nondimensional quantities are primed):

$$t = \frac{\mu_0}{\varepsilon P_0} t', \quad x = Lx', \quad u = \varepsilon \frac{P_0 L}{\mu_0} u', \tag{14}$$

$$p = \frac{12P_0}{\varepsilon} p', \quad y = Ly', \quad v = \varepsilon \frac{P_0 L}{\mu_0} v', \tag{15}$$

$$\sigma = P_0 \sigma', \quad z = \varepsilon Lz', \quad w = \varepsilon^2 \frac{P_0 L}{\mu_0} w'. \tag{16}$$

Here, the pressure p , cross-gap direction z and lateral directions x, y are scaled as in the previous subsection, as is the characteristic velocity $U = \varepsilon P_0 L / \mu_0$. Time is scaled as L/U and the cross-gap velocity w is scaled as εU . The typical size of viscous and viscoelastic stresses is $\mu_0 U / b = P_0$. The velocity gradient and the rate-of-strain tensor are then

$$\nabla \mathbf{v} = \frac{P_0}{\mu_0} \nabla \mathbf{v}', \quad \text{where} \quad \nabla \mathbf{v}' = \begin{pmatrix} \varepsilon u_x & \varepsilon u_y & u_z \\ \varepsilon v_x & \varepsilon v_y & v_z \\ \varepsilon^2 w_x & \varepsilon^2 w_y & \varepsilon w_z \end{pmatrix},$$

and

$$D = \frac{P_0}{\mu_0} D',$$

$$\text{where } D' = \frac{1}{2} \begin{pmatrix} 2\varepsilon u_x & \varepsilon(u_y + v_x) & u_z + \varepsilon^2 w_x \\ \varepsilon(u_y + v_x) & 2\varepsilon v_y & v_z + \varepsilon^2 w_y \\ u_z + \varepsilon^2 w_x & v_z + \varepsilon^2 w_y & 2\varepsilon w_z \end{pmatrix}.$$

To separate the orders of ε , we write these tensors without approximation as

$$\nabla \mathbf{v}' = \mathcal{L}_0 + \varepsilon \mathcal{L}_1 + \varepsilon^2 \mathcal{L}_2, \quad D' = \mathcal{D}_0 + \varepsilon \mathcal{D}_1 + \varepsilon^2 \mathcal{D}_2.$$

There are two nondimensional parameters associated with the scaling given by Eqs. (14)–(16),

$$Re = \varepsilon^2 \frac{\rho UL}{\mu_0} = \varepsilon^3 \frac{\rho P_0 L^2}{\mu_0^2}, \quad \text{Reynolds number;} \tag{17}$$

$$We' = \frac{\lambda U}{\varepsilon L} = \frac{\lambda P_0}{\mu_0}, \quad \text{Weissenberg number.} \tag{18}$$

A natural Deborah number would be defined as $De = \lambda U / L = \varepsilon We'$. We will find it convenient to use the modified Weissenberg number,

$$We = (1 - a^2)^{1/2} 12 We' = (1 - a^2)^{1/2} \frac{12 \lambda P_0}{\mu_0}. \tag{19}$$

Introduce the lateral velocity $\mathbf{u} = (u, v)$, lateral gradient $\nabla_2 = (\partial_x, \partial_y)$ and lateral Laplacian $\Delta_2 = \partial_{xx} + \partial_{yy}$. Then, dropping the primes, the nondimensional momentum conservation equations (2) are

$$Re \frac{D\mathbf{u}}{Dt} = -12 \nabla_2 p + \alpha (\mathbf{u}_{zz} + \varepsilon^2 \Delta_2 \mathbf{u}) + \begin{bmatrix} \sigma_z^{xz} \\ \sigma_z^{yz} \end{bmatrix} + \varepsilon \begin{bmatrix} \sigma_x^{xx} + \sigma_y^{xy} \\ \sigma_x^{xy} + \sigma_y^{yy} \end{bmatrix}, \tag{20}$$

$$\varepsilon^2 Re \frac{Dw}{Dt} = -12 p_z + \varepsilon \sigma_z^{zz} + \varepsilon^2 (\sigma_x^{xz} + \sigma_y^{yz} + \alpha (w_{zz} + \varepsilon^2 \Delta_2 w)), \tag{21}$$

the incompressibility condition (3) is

$$\nabla_2 \cdot \mathbf{u} + w_z = 0, \tag{22}$$

and the constitutive relation (5) with the convected derivative (6) is

$$\begin{aligned} \sigma - We' (\mathcal{L}_0 \sigma + \sigma \mathcal{L}_0^T - (1 - a)(\mathcal{D}_0 \sigma + \sigma \mathcal{D}_0)) \\ = 2(1 - \alpha) \mathcal{D}_0 - \varepsilon \left\{ We' \left(\frac{D\sigma}{Dt} - \mathcal{L}_1 \sigma - \sigma \mathcal{L}_1^T + (1 - a) \right. \right. \\ \left. \left. \times (\mathcal{D}_1 \sigma + \sigma \mathcal{D}_1) \right) - 2(1 - \alpha) \mathcal{D}_1 \right\} + \varepsilon^2 \{ We' (\mathcal{L}_2 \sigma \\ + \sigma \mathcal{L}_2^T - (1 - a)(\mathcal{D}_2 \sigma + \sigma \mathcal{D}_2)) + 2(1 - \alpha) \mathcal{D}_2 \}. \end{aligned} \tag{23}$$

3. Leading order equations

Assume the horizontal velocity \mathbf{u} , the pressure p and the extra stress tensor σ have asymptotic expansions of the form

$$\begin{aligned} \mathbf{u}(\mathbf{x}, t) &= \mathbf{u}^{(0)} + O(\varepsilon), \\ p(\mathbf{x}, t) &= p^{(0)} + O(\varepsilon), \\ \sigma(\mathbf{x}, t) &= \sigma^{(0)} + O(\varepsilon), \end{aligned} \tag{24}$$

and substitute these expansions into Eqs. (20)–(23).

The leading order $O(1)$ contribution to the momentum equations (20) and incompressibility condition (22) are (after dropping the superscripted 0 from the notation) a set of reduced Stokes equations:

$$12 \nabla_2 p = \alpha \mathbf{u}_{zz} + \begin{bmatrix} \sigma_z^{xz} \\ \sigma_z^{yz} \end{bmatrix}, \tag{25}$$

$$p_z = 0, \tag{26}$$

$$\nabla_2 \cdot \mathbf{u} + w_z = 0. \tag{27}$$

The constitutive relations (23) yield the set of linear equations for the stresses:

$$\begin{aligned} \sigma^{xx} - \text{We}'(1+a)\sigma^{xz}u_z \\ = \sigma^{zz} + \text{We}'(1-a)(\sigma^{xz}u_z + \sigma^{yz}v_z) = 0, \end{aligned} \quad (28)$$

$$\begin{aligned} \sigma^{yy} - \text{We}'(1+a)\sigma^{yz}v_z \\ = \sigma^{xy} - \text{We}'\frac{1+a}{2}(\sigma^{xz}v_z + \sigma^{yz}u_z) = 0, \end{aligned} \quad (29)$$

$$\begin{aligned} \sigma^{xz} - \text{We}'\sigma^{zz}u_z + \text{We}'\frac{1-a}{2}((\sigma^{xx} + \sigma^{zz})u_z + \sigma^{xy}v_z) \\ = (1-\alpha)u_z, \end{aligned} \quad (30)$$

$$\begin{aligned} \sigma^{yz} - \text{We}'\sigma^{zz}v_z + \text{We}'\frac{1-a}{2}((\sigma^{yy} + \sigma^{zz})v_z + \sigma^{xy}u_z) \\ = (1-\alpha)v_z. \end{aligned} \quad (31)$$

Equations (28)–(31) can be solved by first finding σ^{xx} , σ^{yy} , σ^{zz} and σ^{xy} in terms of the shear stresses σ^{xz} and σ^{yz} , and then substituting these into Eqs. (30) and (31). After a moderate amount of algebra, the shear-stresses σ^{xz} and σ^{yz} are found to satisfy the equations

$$\mathcal{A} \begin{bmatrix} \sigma^{xz} \\ \sigma^{yz} \end{bmatrix} = (1-\alpha) \begin{bmatrix} u_z \\ v_z \end{bmatrix}, \quad (32)$$

where

$$\mathcal{A} = \begin{pmatrix} 1 + 4Cu_z^2 + Cv_z^2 & 3Cu_zv_z \\ 3Cu_zv_z & 1 + 4Cv_z^2 + Cu_z^2 \end{pmatrix}, \quad (33)$$

and $C = (1-a^2)\text{We}'^2/4$. Note that $C > 0$ as long as the assumption $|a| < 1$ holds. The matrix \mathcal{A} is nonsingular, with a positive determinant,

$$\det \mathcal{A} = (1 + C|\mathbf{u}_z|^2)(1 + 4C|\mathbf{u}_z|^2).$$

The shear stresses, along with the rest of the components of the extra stress tensor, can now be solved from (32) and (28)–(29). They are given by

$$\sigma^{xz} = \frac{1-\alpha}{d}u_z, \quad \sigma^{yz} = \frac{1-\alpha}{d}v_z, \quad (34)$$

$$\sigma^{xx} = \alpha \frac{\text{We}'(1+a)}{d}u_z^2, \quad \sigma^{yy} = \alpha \frac{\text{We}'(1+a)}{d}v_z^2, \quad (35)$$

$$\sigma^{zz} = -\alpha \frac{\text{We}'(1-a)}{d}|\mathbf{u}_z|^2, \quad \sigma^{xy} = \alpha \frac{\text{We}'(1+a)}{d}u_zv_z, \quad (36)$$

where $d = 1 + (1-a^2)\text{We}'^2|\mathbf{u}_z|^2$. Notable is the presence of normal stress differences. This is in contrast to the Hele–Shaw flow of a Newtonian, or a generalized Newtonian fluid, in which case the normal stress differences are zero. However, these normal stress differences only enter at $O(\epsilon)$, and are not present in the leading order reduced Stokes' equations (25)–(26).

Substituting the shear stresses into Eqs. (25)–(26) yields

$$12\nabla_z p = \frac{\partial}{\partial z}(\mu_\alpha((\text{We}/12)^2|\mathbf{u}_z|^2)\mathbf{u}_z), \quad (37)$$

$$p_z = 0, \quad (38)$$

$$\nabla_2 \cdot \mathbf{u} + w_z = 0, \quad (39)$$

as the leading order equations of motion for a JSO fluid in a Hele–Shaw cell. The nondimensional shear viscosity, with both the polymer and the solvent contribution, is

$$\mu_\alpha((\text{We}/12)^2|\mathbf{u}_z|^2) = \frac{1 + \alpha(\text{We}/12)^2|\mathbf{u}_z|^2}{1 + (\text{We}/12)^2|\mathbf{u}_z|^2}, \quad (40)$$

where $\alpha = \mu_s/\mu_0$, and the modified Weissenberg number, We , is given by (19). This agrees with the one-dimensional steady shear flow result.

B. Generalized Darcy's law

The reduced Stokes equations (37)–(39) can be used to derive a generalized Darcy's law, as in Kondic, Palffy-Muhoray and Shelley.¹⁸ The discussion applies to a general shear-rate dependent viscosity function, but we specialize the results to the case of JSO.

Integration of the reduced Stokes equation (37) yields

$$12z\nabla_z p = \mu_\alpha((\text{We}/12)^2|\mathbf{u}_z|^2)\mathbf{u}_z, \quad (41)$$

where we seek flows symmetric about $z=0$, and use the independence of p from z . We would like to express \mathbf{u}_z as a function of $\nabla_z p$, as in the usual Darcy's law. Squaring (41) gives an implicit equation for $|\mathbf{u}_z|^2$ in terms of $z^2|\nabla_z p|^2$. The invertibility of this equation, or lack thereof, is a central issue. A sufficient condition for finding a well-behaved inverse of (41) is that

$$0 < C_0 \leq \mu_\alpha(s^2) + 2s^2\mu'_\alpha(s^2) \leq C_1 < \infty \quad (42)$$

holds for some constants C_0 , C_1 , and all values s (see Appendix A). In this case the inverse viscosity is defined through

$$\mu_\alpha(s^2)s = \zeta \quad \text{whenever} \quad s = \zeta/\bar{\mu}_\alpha(\zeta^2). \quad (43)$$

In the case of JSO, $\mu_\alpha(s^2) = (1 + \alpha s^2)/(1 + s^2)$ with $0 \leq \alpha \leq 1$ a constant, so μ satisfies inequality (42) only for $\alpha > 1/9$. Assuming that inequality (42) holds, Eq. (41) can be inverted uniquely to give

$$\mathbf{u}_z = \frac{12z\nabla_z p}{\bar{\mu}_\alpha(\text{We}^2 z^2 |\nabla_z p|^2)},$$

or

$$\mathbf{u} = \int_{-1/2}^z dz' \frac{12z'\nabla_z p}{\bar{\mu}_\alpha(\text{We}^2 z'^2 |\nabla_z p|^2)}. \quad (44)$$

$\bar{\mathbf{u}}(x,y) = \int_{-1/2}^{1/2} dz \mathbf{u}(x,y,z)$ is the gap-averaged velocity. Gap averaging (44) and the divergence-free condition yields

$$\bar{\mathbf{u}} = \frac{-1}{\bar{\mu}_\alpha(\text{We}^2 |\nabla_z p|^2)} \nabla_z p, \quad \text{and} \quad \nabla_2 \cdot \bar{\mathbf{u}} = 0, \quad (45)$$

where the viscosity function $\bar{\mu}$ is given by

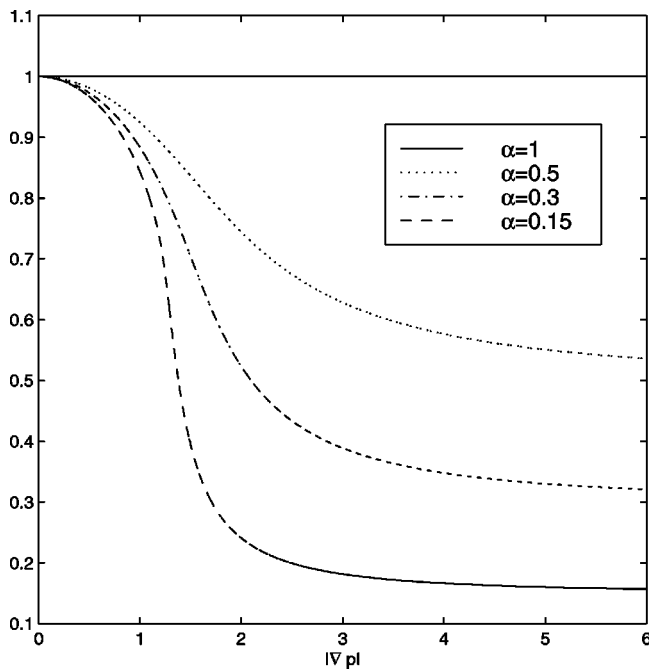


FIG. 3. The effective viscosity $\bar{\mu}$ for some typical values of α with $We = 1$ (changes in We rescale the abscissa).

$$\frac{1}{\bar{\mu}_\alpha(We^2|\nabla p|^2)} = 12 \int_{-1/2}^{1/2} dz \frac{z^2}{\bar{\mu}_\alpha(We^2 z^2|\nabla p|^2)}. \quad (46)$$

Equations (45)–(46) are a generalized Darcy’s law for a non-Newtonian fluid, with the viscosity expressed as a function of $|\nabla p|^2$. The subscript on ∇ and μ , and the bar on \mathbf{u} will be omitted hereafter.

Figure 3 shows $\bar{\mu}_\alpha(We^2|\nabla p|^2)$ for various values of α , with the Weissenberg number simply rescaling the abscissa. We summarize the relations between the four different ‘‘viscosities:’’ μ is the shear viscosity given by (40), $\bar{\mu}$ is the inverse of μ , $\bar{\mu}$ is the gap-average (46) of $\bar{\mu}$, and later we will need $\hat{\mu}$, which is the inverse of the gap-averaged viscosity. For a Newtonian fluid, these would all be equal to the constant μ_0 in dimensional terms, and simply 1 nondimensionally. The ‘‘inverse’’ is always to be taken in the sense discussed above. The viscosity $\bar{\mu}_\alpha(We^2|\nabla p|^2)$ inherits the invertibility and monotonicity of $\mu_\alpha(We^2|\mathbf{u}_z|^2)$. In Appendix A we give a detailed discussion of the properties of the viscosity functions, and an *explicit* expression for $\bar{\mu}$ in the case of JSO.

Remarks. (1) The analysis of this section generalizes immediately to JSO models with multiple relaxation times. Consider a model where the extra stress $\boldsymbol{\sigma}$ is the sum of N modes $\boldsymbol{\sigma}_k$, each satisfying a constitutive relation of the form of Eq. (5). That is, the equations of motion are (2), conservation of mass $\nabla \cdot \mathbf{v} = 0$ and the constitutive relation

$$\boldsymbol{\sigma}_k + \lambda_k \frac{D_a \boldsymbol{\sigma}_k}{Dt} = 2 \eta_k \mathcal{D} \quad (k = 1, \dots, N), \quad \boldsymbol{\sigma} = \sum_{k=1}^N \boldsymbol{\sigma}_k. \quad (47)$$

Here λ_k and η_k are the relaxation time and viscosity of the k -th mode, respectively.

The analysis of Sec. II A can now be applied to Eq. (47) for each mode separately. The reduced Stokes equations in this case are (37)–(39) with the viscosity function $\mu_\alpha = \mu$ given by

$$\mu((We/12)^2|\mathbf{u}_z|^2) = \alpha_0 + \sum_{k=1}^N \frac{\alpha_k}{1 + \beta_k^2(We/12)^2|\mathbf{u}_z|^2}, \quad (48)$$

where $\alpha_0 = \mu_s/\mu_0$, $\alpha_k = \eta_k/\mu_0$, $\beta_k = \lambda_k/\lambda_1$, and $\mu_0 = \mu_s + \sum \eta_k$. The modified Weissenberg number should be defined as in Eq. (19) using the longest relaxation time λ_1 . The generalized Darcy’s law (45) holds now with the effective viscosity $\bar{\mu}$ defined using the inverse viscosity of Eq. (48).

(2) More general constitutive models can be treated. JSO is a special case of the Oldroyd 8 constant model,²⁶

$$\begin{aligned} \boldsymbol{\tau} &= -p\mathcal{I} + \boldsymbol{\sigma}, \\ \boldsymbol{\sigma} + \lambda_1 \frac{D_1 \boldsymbol{\sigma}}{Dt} + \lambda_3(\mathcal{D}\boldsymbol{\sigma} + \boldsymbol{\sigma}\mathcal{D}) + \lambda_5\text{tr}(\boldsymbol{\sigma})\mathcal{D} + \lambda_6(\boldsymbol{\sigma}:\mathcal{D})\mathcal{I} \\ &= 2\mu_0 \left(\mathcal{D} + \lambda_2 \frac{D_1 \mathcal{D}}{Dt} + 2\lambda_4 \mathcal{D}\mathcal{D} + \lambda_7(\mathcal{D}:\mathcal{D})\mathcal{I} \right), \end{aligned}$$

which is the most general differential model linear in the extra stress tensor. Here $\mathcal{A}:\mathcal{B} = \text{tr}(\mathcal{A}\mathcal{B}^T)$, and the upper convected derivative D_1/Dt is given by Eq. (6) with $a = 1$. There are certain restrictions on the constants $\mu_0, \lambda_1 \dots \lambda_7$ for the model to be physically reasonable.²⁶

Applying the scaling (14)–(16) to the Oldroyd 8 constant model yields as the leading order the reduced Stokes equations (37)–(39), but with a different viscosity. Here, the shear-rate dependent viscosity $\mu_\alpha = \mu$ is given by

$$\mu((We/12)^2|\mathbf{u}_z|^2) = \frac{1 + \beta_2(We/12)^2|\mathbf{u}_z|^2}{1 + \beta_1(We/12)^2|\mathbf{u}_z|^2}, \quad (49)$$

where

$$\begin{aligned} \beta_1 &= \alpha_3 + \alpha_5 + \alpha_3(1 - \alpha_3 - \alpha_5) + \alpha_6(1 - \alpha_3 - \frac{3}{2}\alpha_5), \\ \beta_2 &= \alpha_2(\alpha_3 + \alpha_5) + \alpha_4(1 - \alpha_3 - \alpha_5) + \alpha_7(1 - \alpha_3 - \frac{3}{2}\alpha_5), \end{aligned}$$

and $\alpha_j = \lambda_j/\lambda_1$ for $j = 2, \dots, 7$. The modified Weissenberg number should be defined as in Eq. (19) using λ_1 instead of λ . Note that no generality is gained by using the Oldroyd 8 constant model instead of JSO in the present context; although the Oldroyd 8 constant model yields more general expressions for the extra stresses, the resulting reduced Stokes equations are the same as with JSO, with the shear-rate dependent viscosity of the same form.

(3) The model used by Bonn *et al.*,^{27,28} similar to Eq. (45) but with the viscosity depending on $|\mathbf{u}|$, now follows by using the viscosity $\hat{\mu}$ instead of the viscosity $\bar{\mu}_\alpha(We^2|\nabla p|^2)$ in Eq. (45), thereby expressing ∇p explicitly in terms of \mathbf{u} . In this case, the functional form is such that this inversion can always be accomplished. We consider Eq. (45) to be the \ddot{y} -more natural form of the flow equations; it leads to a boundary value problem for pressure, as in the Newtonian case.

(4) Darcy’s law could be formulated in the same manner with a ‘‘power-law’’ viscosity $\mu(|\mathbf{u}_z|^2) = (|\mathbf{u}_z|^2)^\alpha$. The pa-

parameter $|\alpha| < 1/2$ is negative for a shear-thinning fluid. Darcy’s law is still given by Eq. (45), with the effective viscosity $\bar{\mu}$ now given by

$$\bar{\mu}_\alpha(|\nabla p|^2) = \frac{3+4\alpha}{3(1+2\alpha)} \left(\frac{1}{4} |\nabla p|^2 \right)^{\alpha/(1+2\alpha)}. \quad (50)$$

This model was used by Poiré and Ben Amar,^{20,21} who studied the Saffman–Taylor instability of a weakly shear-thinning power-law fluid ($\alpha \ll 1$) in a channel geometry. Lindner, Bonn and Meunier²² have also used this expression to describe their experimental results.

Boundary conditions on the pressure. Applying the divergence-free condition to the generalized Darcy’s law yields

$$\nabla \cdot \left(\frac{1}{\bar{\mu}_\alpha(\text{We}^2 |\nabla p|^2)} \nabla p \right) = 0, \quad (51)$$

which is a nonlinear BVP for the pressure. As a boundary condition we will use in this work the Laplace–Young condition:

$$[p] = \text{Ca}^{-1} \kappa, \quad (52)$$

for the pressure jump $[p]$, where κ is the interfacial curvature, $\text{Ca} = 12\varepsilon^{-2} \mu_0 U / \gamma$ is a (modified) capillary number, and γ is a surface tension parameter. This boundary condition is typically used, and has been justified,^{29,30} for Newtonian Hele–Shaw flows. For the parametric regime which we study—moderate Weissenberg and capillary numbers—the current state of theoretical and experimental evidence suggests that this boundary condition remains appropriate. Further, as our simulations do capture important qualitative features observed in experiment, our results might be interpreted as an *a posteriori* justification for this assumption. Nonetheless, as the question of boundary conditions in non-Newtonian flows is a complicated one, we give a brief review of what seem to be the relevant issues.

The derivation of the bulk fluid equation (1) assumes a separation of length-scales into a large lateral length scale L and a small gap-thickness b so that $\varepsilon = b/L \ll 1$. No such separation of length-scales is available near the meniscus, where in fact the flow is fully three dimensional (see Smith, Wu, Libchaber, Moses and Witten,³¹ and Tabeling, Zocchi and Libchaber³²), and at which the fluid satisfies a stress jump condition. An analysis of the flow near the meniscus is therefore required to derive a consistent approximation to the boundary conditions on the gap-averaged pressure.

It is known that an air bubble displacing a fluid in a Hele–Shaw cell leaves behind a thin residual film. The thickness of this film varies with bubble velocity and so gives rise to variations in the pressure jump across the meniscus. An analogous problem is that of a long air bubble displacing a fluid in a capillary tube,^{33,29,34,30} which for the Newtonian case was analyzed by Bretherton³³ by expanding in a very small capillary number $\widetilde{\text{Ca}} = \mu U / \gamma \ll 1$. This analysis was generalized to Newtonian Hele–Shaw flow by Park and Homsy,²⁹ again for small $\widetilde{\text{Ca}}$, who showed that the Laplace–Young condition gave the leading order contribution. Reinelt and Saffman^{30,34} removed the small $\widetilde{\text{Ca}}$ restriction through

direct numerical solution of the flow, and determined the correct pressure boundary conditions up to $\widetilde{\text{Ca}} = O(1)$. Reinelt³⁵ studied viscous fingering in a channel Hele–Shaw cell geometry, and extended the work of McLean and Saffman³⁶ by using the improved boundary conditions: his analysis recovered the experimentally observed finger widths. (These improved boundary conditions have not been applied in numerical simulations of radial Hele–Shaw flow and, in fact, are not generally used.) In this work, we concentrate on the case $\widetilde{\text{Ca}} \ll 1$, and do not consider these corrections.

In the case of a non-Newtonian fluid in a Hele–Shaw cell, only partial theoretical results are available. Ro and Homsy³⁷ generalized the analysis of Park and Homsy,²⁹ and found corrections to the pressure boundary condition for an Oldroyd-B fluid model.²⁶ However, they do not consider terms depending on the lateral curvature, and only account for changes in the thickness of the residual film.

We remark that Wilson³⁸ has used *ad hoc* boundary conditions in an attempt to account for normal-stress effects in his study of the non-Newtonian Saffman–Taylor instability. He derived a normal-stress jump condition at the interface by assuming the stress distribution in the bulk fluid can be extended up to the interface; however Ro and Homsy,³⁷ working in the limit $\widetilde{\text{Ca}} = \mu_0 U / \gamma \ll 1$, show that this assumption is incorrect.

Several experimental studies have identified normal-stress differences as being important in some instances of non-Newtonian Hele–Shaw flow (see Smith, Wu, Libchaber, Moses and Witten,³¹ Gauri and Koelling³⁹ and Huzyak and Koelling⁴⁰). However, this is highly dependent on the parametric regime considered. Indeed, the aforementioned experiments reveal that the Newtonian and non-Newtonian case yield an almost identical response if the capillary number and Weissenberg number are moderate, as in the present paper.

Gauri and Koelling³⁹ study the flow dynamics at the tip of the meniscus of a long air bubble that displaces a viscoelastic fluid with a constant shear-viscosity. Their experiments are characterized in terms of a capillary number $\widetilde{\text{Ca}}$ and a Deborah number De ,

$$\text{De} = \frac{\lambda U}{b} = \text{We}' = \frac{\text{We}}{12\sqrt{1-a^2}} \approx \frac{1}{4} \text{We},$$

where U/b is the wall shear-rate in Hele–Shaw flow, and the last approximative equality applies for $|a| \approx 0.9$. They find two distinct flow patterns at the tip of the meniscus, as sketched already by Taylor:⁴¹ a complete bypass flow, and a recirculation flow. When $\text{De} \geq 1$ the flow completely bypasses the tip of the bubble, creating a strong extensional flow field. The response of the non-Newtonian fluid changes dramatically at $\text{De} \approx 1$. This transition could be perhaps attributed to a “coil–stretch” transition (De Gennes⁴²), which occurs due to the sudden uncoiling of polymer strands in the strong extensional flow near the tip of the meniscus for $\text{De} \geq 1$.

However, such behavior is an example of the response in a particular parametric regime. For *moderate* $\text{De} < 1$ and

$Ca < 10^3$, Gauri and Koelling³⁹ show that there is no strong extensional flow near the tip. Further, for $De < 0.35$, the flow field near the meniscus tip for non-Newtonian fluids was similar to that for Newtonian fluids, and the thicknesses of their residual films were nearly identical. In our numerical studies (Sec. V) we concentrate on flows where $Ca < 10^3$, and the modified Weissenberg number is moderate, $We < 0.5$ ($De < 0.125$). This parametric regime should be below the transition to bypass flow and a possible “coil–stretch” response.

In a channel Hele–Shaw cell, Smith *et al.*³¹ studied the properties of Saffman–Taylor fingers in very dilute solutions of polystyrene dissolved in a Newtonian solvent. They found a transition to narrow fingers when the modified capillary number $Ca \sim 10^3$, and the shear rate U/b was comparable to the inverse of the polymeric relaxation time λ (estimated using Zimm theory). Their analysis³¹ yields again the critical Deborah number $De \approx 1$, at which the abrupt change in response is attributed to a “coil–stretch transition.” And again, for the capillary numbers considered herein, Smith *et al.*³¹ found an essentially Newtonian response.

Although it is reasonable to assume that in this parametric regime normal-stress effects are negligible near the tip of the meniscus, it is possible that viscoelastic effects in the thin film region become important.³⁷ However, for moderate Weissenberg numbers ($We' < 1$), Gauri and Koelling³⁹ and Huzyak and Koelling⁴⁰ show that in a purely elastic polymeric (Boger) fluid the residual film thickness scales almost identically in \tilde{Ca} for Newtonian and non-Newtonian fluids: the Ro and Homsy analysis³⁷ suggests in this case that the non-Newtonian effects at the meniscus are negligible, and Newtonian boundary conditions are applicable. Hence, it seems reasonable to neglect elastic effects at the interface in the parametric regime in which we are interested.

The effect of shear-thinning near the meniscus has been less researched: in light of theoretical studies (Ro and Homsy³⁷ and Fast⁴³) it is possible that shear-thinning gives rise to corrections to the Laplace–Young condition. A more detailed analysis is clearly warranted: It is likely that a full numerical simulation, as performed by Reinelt and Saffman³⁰ for Newtonian fluids, is required to settle the question of shear-thinning and viscoelastic non-Newtonian contributions to the pressure boundary conditions.

C. Dynamics of an expanding bubble

We now consider the evolution of a gas bubble expanding under an applied pressure into a non-Newtonian fluid in a radial Hele–Shaw cell. The fluid domain is taken to be an annular region Ω bounded by an inner boundary Γ_i and an external boundary Γ_e . Let the inner and outer boundary be given by the curve $\mathbf{x}_{i,e}(\beta, t)$, respectively, where we assume β to be the Lagrangian parametrization of the curve.

We will study initial data, for an expanding interface, which is a small perturbation from a circle. Accordingly, in defining the nondimensional parameters, Ca and We , we use as characteristic length and velocity scales the initial bubble radius R_0 and initial velocity \dot{R}_0 .

The full evolution problem for Ω is the nonlinear BVP for the pressure,

$$\nabla \cdot \left(\frac{1}{\bar{\mu}_\alpha (We^2 |\nabla p|^2)} \nabla p \right) = 0, \quad p|_{\Gamma_i} = 1 - Ca^{-1} \kappa_i, \quad p|_{\Gamma_e} = Ca^{-1} \kappa_e, \quad (53)$$

and the kinematic condition,

$$\frac{\partial \mathbf{x}_{i,e}}{\partial t}(\beta, t) = \mathbf{u}(\mathbf{x}_{i,e}(\beta, t), t), \quad (54)$$

which states that the boundaries are material curves.

Remarks: (1) Nonlinear BVPs similar to Eq. (53) arise as the steady states of nonlinear conservation laws in many other physical contexts, such as gas dynamics⁴⁴ and magnetostatics.⁴⁵ The solvability of Eq. (53) is established in Appendix A3 using classical results; inequality (42) is also a sufficient condition for Eq. (53) to have a unique solution.

(2) Consider a finite patch of fluid, denoted by Ω with boundary Γ , surrounded by gas at uniform pressure (set to zero). Then the length of the boundary curve decreases with time, so the dynamics is curve shortening. To show this, the nonlinear BVP (53) with the Laplace–Young boundary condition must be augmented with the kinematic condition (54) where the boundary curve \mathbf{x} is parametrized with the Lagrangian parameter β . The velocity is obtained from the pressure through Darcy’s law (1). This free-boundary problem describes the relaxation of the bubble under capillary forces. A direct calculation shows that the length \mathcal{L} of the boundary curve decreases in time since

$$\frac{d\mathcal{L}}{dt} = -Ca \int_{\Omega} \frac{|\nabla p|^2}{\bar{\mu}_\alpha (We^2 |\nabla p|^2)} dA < 0.$$

(3) The Weissenberg number could be removed from the problem by rescaling Eqs. (53), (54) and (46) as $L \rightarrow WeL$, $t \rightarrow We^2 t$, and $Ca \rightarrow Ca/We$. However, we retain a We dependence in what follows to keep a fixed physical length-scale for our initial data.

III. LINEAR STABILITY ANALYSIS

We study the linear stability of a circular bubble of radius $R(t)$, which is perturbed by a small azimuthal disturbance, and expands into a non-Newtonian fluid in an unbounded Hele–Shaw cell. For simplicity, we impose in this section a constant mass flux as the driving force, so that the area $S(t)$ of the bubble satisfies $S_t/2\pi = RR_t = 1$. The nondimensionalization is chosen so that $R(0) = 1$, $R_t(0) = 1$.

The bubble is centered at the origin and the position \mathbf{R} of the interface Γ is given by

$$\mathbf{R}(\theta, t) = R(t)[1 + \epsilon \eta(\theta, t)] \hat{\mathbf{r}}, \quad (55)$$

where $\epsilon \ll 1$, and η is the perturbation. Assuming a purely radial flow far from the expanding bubble, the far-field boundary condition simplifies to

$$p(r) \sim -\ln r, \quad \text{as } r \rightarrow \infty,$$

similarly to the Newtonian case.

Since $\eta(\theta, t)$ can be written as a Fourier series in the azimuthal angle θ , and the linearized equations are separable, we consider without loss of generality a perturbation of the form $\eta(\theta, t) = N(t) \cos m\theta$, where m is a wave number, and $N(t)$ is the amplitude of the perturbation. We derive an expression for the growth rate $\sigma_m = N_t/N$ for a weakly non-Newtonian fluid, as well as for a general shear-thinning fluid.

A. Weakly non-Newtonian limit

We start by considering the weakly non-Newtonian limit $We^2 \ll 1$, where we can obtain an explicit expression for the growth rate. This limit can be attained experimentally by choosing a fluid with a short relaxation time λ , or by choosing P_0 to be small, as is suggested by (19).

Expanding the viscosity function (40) for JSO in $We^2 \ll 1$ yields

$$\mu_\alpha (We^2 |\mathbf{u}_z|^2) = 1 - We^2 (1 - \alpha) |\mathbf{u}_z|^2 + O(We^4).$$

All dependency on the specific viscosity function is contained in the parameter α . By introducing in Eq. (41) a small We expansion for $p = p_0 + We^2 p_1$ and $\mathbf{u} = \mathbf{u}_0 + We^2 \mathbf{u}_1$, integrating and gap-averaging as in Sec. II B, we obtain the two term hierarchy,

$$\mathbf{u}_0 = -\nabla p_0, \quad \nabla \cdot \mathbf{u}_0 = 0, \tag{56}$$

$$\mathbf{u}_1 = -\nabla p_1 - \frac{3(1-\alpha)}{20} |\nabla p_0|^2 \nabla p_0, \quad \nabla \cdot \mathbf{u}_1 = 0, \tag{57}$$

with the boundary conditions

$$p_0|_\Gamma = -Ca^{-1} \kappa, \quad p_1|_\Gamma = 0, \tag{58}$$

$$p_0 \rightarrow -\ln r, \quad p_1 \rightarrow C, \quad \text{as } r \rightarrow \infty. \tag{59}$$

The constant C is determined as a part of the solution.

By solving the perturbation pressure p_1 from Eqs. (56)–(59) and using the kinematic boundary condition, we find the instantaneous growth rate

$$\begin{aligned} \sigma_m = & -1 + m \left(1 + \mathcal{B} \frac{m-1}{m+1} \right) \\ & + Ca^{-1} m(1-m^2) \left(1 + \mathcal{B} \frac{2m}{m+1} \right). \end{aligned} \tag{60}$$

In this weakly non-Newtonian limit, the non-Newtonian character of the fluid is contained in the single small positive parameter $\mathcal{B} = (3/20)(1-\alpha)We^2$.

In the absence of surface tension ($Ca^{-1} = 0$), the growth-rate σ_m is always positive and grows essentially linearly with the wave number m , making the system ill-posed. Introducing surface tension ($Ca^{-1} > 0$) stabilizes the large wave numbers, and yields a band of unstable modes at intermediate wave numbers. This is similar to the case of a Newtonian fluid.

The shear-thinning of the fluid has several effects on the growth rate. The wave number of maximum growth for a Newtonian fluid is given by⁴⁶

$$m_{\max}^{\text{Newt}} = \sqrt{\frac{1+Ca}{3}}. \tag{61}$$

From Eq. (60), one can obtain an explicit solution for the wave number m_{\max} with a maximal growth rate in the weakly non-Newtonian case. This expression is rather complex, but in the limit $Ca^{-1} \ll 1$ it simplifies to

$$m_{\max} \approx m_{\max}^{\text{Newt}} \left(1 - \frac{\mathcal{B}}{2} \right). \tag{62}$$

The maximal growth rate is increased by shear-thinning if $Ca > 17$. Typical experimental values of the capillary number are much larger than this.¹² Similarly, the critical wave number m_c , the maximum wave number for which the growth rate is still positive, is shifted towards lower wave numbers as shear-thinning is increased. We find that the relation $m_c^{\text{Newt}} = \sqrt{3} m_{\max}^{\text{Newt}}$ holds approximately for a shear-thinning fluid as well.

To summarize, in the weakly non-Newtonian limit shear-thinning decreases the wave number of maximum growth, increases the maximum growth rate and tightens the band of unstable modes. This suggests an increased selectivity of wavelengths in the pattern formation problem. For shear-thickening fluids, the results are reversed: the growth rate for the wave number of maximum growth is decreased for all reasonable values of the capillary number, and the wave numbers of maximum and critical growth are increased.

B. Linear stability: General case

Let us now return to the general case [$We = O(1)$] of a non-Newtonian fluid whose viscosity is given by Eq. (40). We do not obtain an explicit expression for the growth rate in this case, but can find the growth rates numerically.

In the absence of perturbations, the radius $R(t)$ of a circular bubble evolves as $R_t = 1/R$, since we impose a constant mass-flux at infinity. The corresponding velocity field is given by $\bar{\mathbf{u}}(r, t) = \hat{\mathbf{r}}/r$. We define the pressure \bar{p} through

$$\bar{p}_r(r) = -\hat{\mu}(We^2/r^2) \frac{1}{r}, \quad \bar{p}(R(t)) = -\frac{1}{Ca R(t)},$$

by expressing the viscosity as a function of \mathbf{u} . The connection of $\hat{\mu}$ to the previously defined viscosities is discussed in Sec. II B.

The perturbation of the interface induces perturbations to the pressure and velocity fields, which we expand as

$$\mathbf{u}(r, \theta, t) = \bar{\mathbf{u}}(r) + \varepsilon \tilde{\mathbf{u}}(r, \theta, t),$$

$$p(r, \theta, t) = \bar{p}(r, t) + \varepsilon \tilde{p}(r, \theta, t).$$

By expanding Darcy’s law (45) and the boundary conditions (53) in ε , we obtain for the pressure perturbation \tilde{p} the linear boundary value problem,

$$\nabla \cdot \left[\frac{\bar{\mu} - 2 We^2 \bar{\mu}' \nabla \bar{p} \nabla \bar{p}^T}{\bar{\mu}^2} \nabla \tilde{p} \right] = 0, \quad \text{for } r > R(t), \tag{63}$$

$$\tilde{p}(R, \theta) = -\bar{p}_r(R) R \eta + \frac{1}{R Ca} (\eta + \eta_{\theta\theta}), \tag{64}$$

$$\tilde{p} \rightarrow 0, \quad \text{as } r \rightarrow \infty. \tag{65}$$

Here $\bar{\mu} = \bar{\mu}(We^2 \bar{p}_r^2)$, and $\bar{\mu}'$ is defined analogously.

The separation of variables with $\bar{p}(r, \theta, t) = P(t, m)f(r, m)\cos(m\theta)$ leads to the linear two-point boundary-value problem,

$$\frac{1}{r} \frac{\partial}{\partial r} \left[r \left(\frac{\bar{\mu} - 2We^2 \bar{\mu}' \bar{p}_r^2}{\bar{\mu}^2} \right) f_r \right] - \frac{m^2}{r^2 \bar{\mu}} f = 0, \quad (66)$$

$$f(r=R) = 1, \quad (67)$$

$$f \rightarrow 0, \text{ as } r \rightarrow \infty. \quad (68)$$

The factorization of \bar{p} was chosen so that $f(R)=1$, which requires

$$P(t) = \left(\hat{\mu}(We^2/R(t)^2) + \frac{1}{R(t)Ca}(1-m^2) \right) N(t),$$

for the perturbation pressure to satisfy the boundary condition (64).

Equation (66) approaches its Newtonian counterpart ($\bar{\mu} = 1, \bar{\mu}' = 0$) as $r \rightarrow \infty$, so we expect

$$f_r(r) \approx -\frac{m}{r} f(r), \quad (69)$$

to hold for $r \gg 1$. We impose Eq. (69) at a large, but finite radius $r = r_{out}$, instead of Eq. (68) when solving the two-point boundary value problem (66)–(68) numerically. Together with the kinematic boundary condition, this completes the formulation of the problem, and the growth rate σ_m is given by

$$\sigma_m = \frac{1}{R} \left[-R_t - \left(\frac{\bar{\mu}_1 - 2We^2 \bar{\mu}'_1 \bar{p}_r^2(R)}{\bar{\mu}_1^2} \right) \times \left(\bar{\mu}_1 + \frac{1}{R Ca} (1-m^2) \right) f_r(R) \right], \quad (70)$$

where $\bar{\mu}_1 = \bar{\mu}(We^2 \bar{p}_r(R(t))^2)$, $\bar{\mu}'_1 = \bar{\mu}'(We^2 \bar{p}_r(R(t))^2)$, and f_r is obtained through numerical integration of Eqs. (66), (67) and (69).

C. Discussion

In Fig. 4 we show results of linear stability analysis for the general shear-thinning fluid. First, in Fig. 4(a) decreasing the shear-thinning parameter α leads to an increased growth rate of the wave number of maximum growth, and its shift toward lower wave numbers, as predicted by the weakly non-Newtonian model. Comparing Fig. 4(a) with Fig. 4(b), we see that an increase of We reduces the range of unstable wave numbers considerably; one might expect increased stability of short wavelengths for large We . Another point to note is that, contrary to Fig. 4(a), decreasing α does not necessarily lead to an increase of the growth rate of the mode of maximum growth. Still, strongly shear-thinning fluids do show increased growth rates in the range of We mostly considered in this paper ($We < 0.5$). The comparison of Figs. 4(a),(b) with Figs. 4(c),(d) show the role of Ca ; an increase of Ca makes shorter wavelengths unstable, increases the growth rate of unstable wave numbers, and augments the effect of shear-thinning.

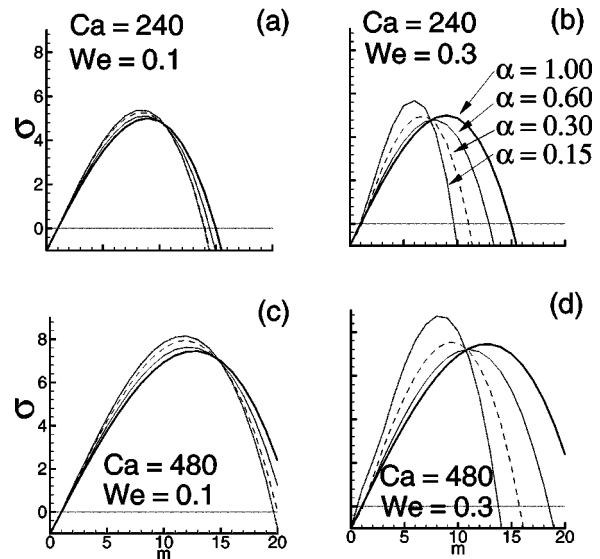


FIG. 4. The growth rate σ for general shear-thinning fluid (see the text).

Increased wavelength selection, resulting from shear-thinning, as well as the stabilization of short wavelengths, encourages the idea that shear-thinning might lead to the suppression of tip-splitting. However, due to the intrinsic nonlinearity of the problem, we prefer not to make any definite conclusions based on linear theory alone. Linear stability analysis does, however, provide us with the basic understanding of the problem and guidance in performing fully nonlinear time dependent simulations of an expanding bubble. This is the subject of the next section.

IV. NUMERICAL SIMULATION

In this section, we discuss the discretization and numerical solution of the full evolution problem (53)–(54) of a gas bubble expanding into a non-Newtonian fluid. As initial data, we take the interior interface Γ_i as a circle perturbed with a single azimuthal mode, and the outer boundary Γ_e as a circle.

The kinematic condition (54) can be viewed roughly as an ODE for the boundary of the bubble, with the right hand side a complicated and nonlocal function of the boundary of the domain. The numerical solution of (53)–(54) using an explicit time-integration scheme can then be outlined as follows.

- (1) Given the boundary position, solve for the pressure from (53).
- (2) Find the velocity from the pressure using Darcy’s law (45).
- (3) Find the new boundary position according to (54).

The full evolution problem is much harder to solve numerically than the corresponding problem for a Newtonian fluid, where the pressure is harmonic. In that case, boundary integral methods coupled with the “small-scale decomposition” (Hou, Lowengrub and Shelley⁶) make it possible to solve the problem efficiently. In the non-Newtonian case, the pressure satisfies the nonlinear BVP (53), and must be solved

for in the whole domain. Since the problem is driven by the curvature of the boundaries, high spatial resolution is required. Further, there is a severe stability constraint on the time-step, leading to a computationally intensive problem. For efficiency, we impose a four-fold symmetry on the initial bubble shape, and the solution.

Methods for solving the equation for the pressure are presented in Sec. IV A. Issues related to evolving the boundaries are addressed in Sec. IV B.

A. Pressure solver

The solution of the pressure requires solving a nonlinear elliptic PDE in a complicated evolving geometry. Although solution methods for problems of this type have been considered in the literature, for example by Concus,⁴⁵ they have typically been for steady state calculations, where efficiency was not as critical as in the present problem.

We use a Lagrangian grid which conforms to the interfaces and moves with the fluid. The fluid domain is mapped onto an annulus, where the the nonlinear BVP is discretized using finite differences, and the resulting system of equations is solved. We introduce on the annulus the coordinates (ζ, η) , where ζ is a ‘‘radial’’ coordinate, and η is a 2π -periodic azimuthal coordinate, so that (ζ, η) is mapped to the point (x, y) in the fluid domain according to

$$\begin{cases} x = x(\zeta, \eta), \\ y = y(\zeta, \eta), \end{cases} \text{ with Jacobian } J = \begin{bmatrix} x_\zeta & y_\zeta \\ x_\eta & y_\eta \end{bmatrix}. \quad (71)$$

The inner boundary Γ_i corresponds to $\zeta = 1$, and the outer boundary Γ_e to $\zeta = 2$. Formulas are modified when expressed in the new coordinates, for example, $\nabla p(x, y) = J^{-1} \bar{\nabla} p(\zeta, \eta)$, where $\bar{\nabla}$ is the gradient with respect to the annular variables. In particular, we solve

$$\mathcal{N}(p) = \nabla \cdot \left\{ \frac{\nabla p}{\bar{\mu}(\text{We}^2 |\nabla p|^2)} \right\} = 0 \text{ in } \Omega,$$

and

$$p = f \text{ on the boundary } \partial\Omega, \quad (72)$$

for a given f , with \mathcal{N} expressed in the annular variables. We present the numerical methods in the original variables (x, y) for clarity, but in practice, our computations are carried out in the annular variables.

We use two iterative methods to solve the BVP (72). Both iterations reduce the nonlinear problem (72) to a sequence of linear elliptic BVP’s. The solution of these linear problems is an issue in itself.

Typically, we use Newton’s method,⁴⁷ for which a linearization, or Fréchet-derivative, of \mathcal{N} has to be calculated. One then solves at each iteration the linear, variable coefficient elliptic BVP,

$$\begin{aligned} \mathcal{N}'(p_n) p_{n+1} &= \mathcal{N}'(p_n) p_n - \mathcal{N}(p_n), \text{ in } \Omega, \\ p_{n+1} &= f \text{ on } \partial\Omega, \end{aligned}$$

for the approximation p_{n+1} . Here the Fréchet-derivative \mathcal{N}' is given by

$$\mathcal{N}'(p)q = \nabla \cdot \left\{ \frac{\bar{\mu} - 2 \text{We}^2 \bar{\mu}' \nabla p \nabla p^T}{\bar{\mu}^2} \nabla q \right\}.$$

Since this linear problem is solved approximately in practice, the convergence of the resulting scheme is typically less than quadratic.⁴⁸ Newton’s method can be quite sensitive to the choice of the initial guess, and can diverge if the initial guess is poor. We encounter this problem in the simulations when the interface begins to develop structure. In this case, we switch to the projection-iteration scheme.

The projection-iteration scheme⁴⁹ for the solution of (72) is defined by

$$\Delta p_{n+1} = \Delta p_n - k \mathcal{N}(p_n), \text{ in } \Omega, \quad p_{n+1} = f \text{ on } \partial\Omega,$$

where $k > 0$ is a parameter of the method. The iteration can be shown to converge for any initial guess p_0 , provided that the parameter k is chosen appropriately. However, sufficient conditions that guarantee convergence for a range of k appear to be far from tight, and we find that the convergence of the method can be enhanced considerably by choosing the value of k dynamically. This value may lay outside of the range of theoretically guaranteed convergence.

Finite differencing of the linear BVP produces a sparse, but nonsymmetric linear system of equations for the unknown pressure at the grid points. After a comparison with a number of iterative schemes,⁵⁰ we chose to use the biconjugate gradient method with a diagonal preconditioner to solve the linear equations.

B. Moving the interface

As is typical for curvature driven free boundary flows, the computational problem is exceedingly stiff. The size of a time-step is strongly constrained by numerical stability. We find that the stability constraint is always more restrictive than say resolving the time-scale of the fastest growing linear mode. As is known for the Newtonian case,⁶ and is suggested by our weakly non-Newtonian linear stability analysis (Sec. III), the step-size Δt for an explicit scheme should satisfy

$$\Delta t < C (\Delta s_{\min})^3, \quad (73)$$

where Δs_{\min} is the minimum spacing of mesh points on the interfaces, and C is a constant. We observe and enforce this constraint in our code, using an empirically determined value for C . For time-evolution, we use an explicit, two-stage Runge–Kutta method with repeated Richardson extrapolation. The step-size is sometimes reduced after taking two half-steps and comparing the error with that obtained after a full step. An implicit time-stepping scheme would presumably ameliorate the stability constraint, but the implementation of such a scheme in the present context is difficult. The severe stability constraint (73) is a primary obstacle to long-time simulation of the evolution problem (53)–(54).

Remarks. (1) Number of grid points. The length of the interface increases by more than two orders of magnitude

during the simulations. A large number of points would be desirable for resolution, whereas a small number of points would be preferred to alleviate the stability constraint. To strike a balance, we begin typically with 64 points on a quarter of an interface in the azimuthal direction, with the resolution increased as needed up to 512 points. In the radial direction, we use a fixed number of points, typically 100–150. A lower resolution leads to a rapid loss of accuracy.

(2) *Time extrapolation.* The pressure solver, in particular Newton's method, is quite sensitive to the initial guess. Since the time steps are relatively small because of the stability constraint, we can find a good initial guess for the solution at the next time step by extrapolating the results from two previous time steps. However, when the bubble develops more structure, this initial guess might not be good enough to ensure the convergence of Newton's iteration. In this case, we switch to the projection-iteration method.

(3) *Clustering of grid points.* The Lagrangian discretization tends to move grid points away from the tips of the forming fingers, and into the fjords. This clustering is undesirable; the flow near the tips is left underresolved, and the fjords are overresolved. The unnecessary clustering of points in the fjords also worsens the stability constraint. Consequently, regridding to equally spaced points in the azimuthal variable is performed when needed. An alternative approach would be to impose this dynamically by adding an azimuthal velocity component to the velocity of the mesh points so as to keep the grid points equally spaced (see Hou *et al.*⁶).

(4) *Second order accuracy.* Our numerical scheme is second order accurate in time and space. Evaluating the velocity from a pressure field through (45) requires special attention at the boundaries. We find that calculating a finite difference approximation to a radial (or ζ) derivative of the pressure at the boundaries by extrapolating from two interior levels of points, as is commonly done, leads to a nonsmooth radial error in the velocity: Although the one-sided approximation used at the boundaries and the centered approximation used away from the boundaries are both second order accurate, the one-sided approximation has a much larger constant multiplying the leading order error. To avoid this problem, we have devised an improved extrapolation scheme which uses three layers of points in the interior to calculate the derivatives at the boundaries. The new scheme yields second order accuracy, but with a smooth error in the velocity field. We have verified the second-order accuracy in space and time of our code by varying the spatial and temporal resolutions, and estimating the numerical errors.

V. DISCUSSION OF THE RESULTS

In this section we discuss the simulational results. First, a study of the influence of shear-thinning fluid behavior on pattern formation is given. A more detailed analysis of the influence of nondimensional parameters in the problem follows, as well as some comments on the effect of using different effective viscosity functions. Finally, we address the question of the dependence of emerging length-scales on the flow and fluid characteristics.

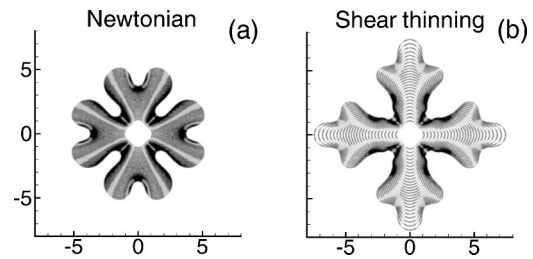


FIG. 5. The snap-shots of the evolving bubble interface for (a) Newtonian fluid and (b) strongly shear-thinning fluid ($Ca=480$ for both simulations, $\alpha=0.15$, $We=0.15$ for shear-thinning one).

A. The effect of shear-thinning on the dynamics of the interface

From experiment,⁴⁶ theory^{51–53,7} and simulation,⁶ the basic elements of pattern formation are well understood for a gas bubble expanding into a Newtonian fluid in a radial Hele–Shaw cell. Very roughly, a perturbation of the bubble interface grows outwardly into an expanding petal. When this petal's radius of curvature exceeds the wavelength of an unstable mode, it “tip-splits” into two nascent petals, which themselves broaden and split. This repeated process yields an interface described by a population of branches and fjords, and whose evolution is characterized by strong competition among the branches, with some branches being “shielded” and retracting, and others advancing farther into the fluid. Clearly, if tip-splitting can be suppressed a much different pattern morphology will follow.

The beginnings of the pattern formation scenario for a Newtonian fluid are seen in Fig. 5(a), which shows the simulation of an expanding bubble, plotted at equal time intervals. The initial shape is a circle perturbed by an $m=4$ cosine mode of amplitude a , where $a/R_0=0.1$. In Fig. 5(a) we observe the unstable mode growing into a petal (say, about $\theta=0$), which widens, and then splits into two as its radius of curvature increases. (Again, much more developed patterns can be computed with higher accuracy using boundary integral methods.⁶)

The bubble evolution in a strongly shear-thinning fluid is strikingly different, as is illustrated in Fig. 5(b). This simulation has the same capillary number as the Newtonian simu-

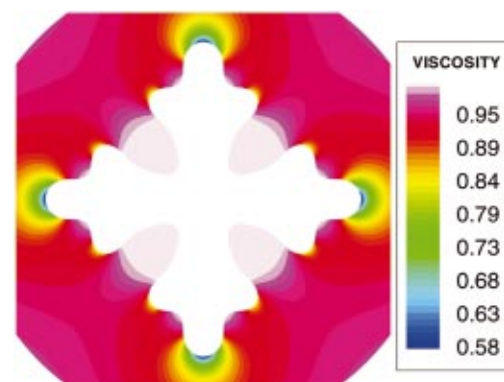


FIG. 6. (Color) Contour plot of the viscosity of the driven fluid ($We=0.15$, $\alpha=0.15$, $Ca=480$).

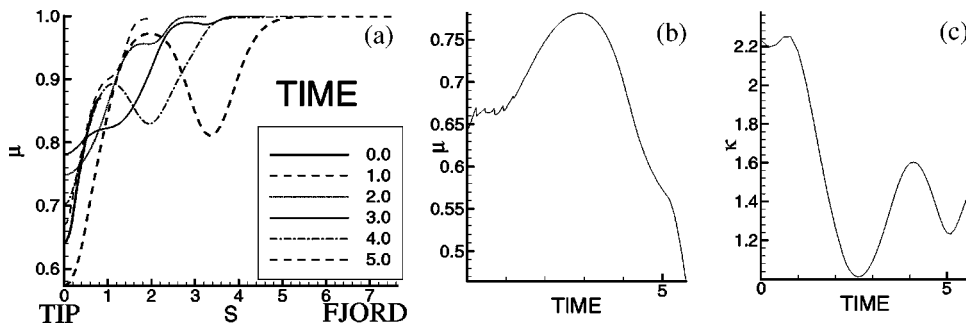


FIG. 7. (a) The viscosity of the fluid along the interface for a nontip-splitting finger (S is the arc length measured from the tip); (b) the time evolution of the viscosity at the tip; (c) the time evolution of the curvature of the tip.

lation, and again has initial data unstable to the Saffman–Taylor instability. The first and plainest effect of shear-thinning is to suppress the tip-splitting of the outwardly growing petal. As the petal expands outwards, it appears to near a splitting, but then “refocuses,” leaving behind “side-branches,” and continues to grow outwards. This refocusing occurs twice during the shown course of the evolution, with the larger (and later) side-branches themselves beginning to grow outwards and giving the impression of a trifurcation of the petal, rather than the bifurcation associated with tip-splitting in the Newtonian flow. We note that the presence of a single mode ($m=4$) at $t=0$ necessarily influences the shape of evolving patterns by imposing a symmetry which is not present in a physical experiment. By performing additional simulations, characterized by different modes m and also by a combination of different m ’s, we have verified that the main results (in particular, the phase diagrams of Sec. VB, and the length-scale results of Sec. VD) are not modified by this assumption.

Figures 6, 7 and 8 provide us with some intuitive understanding of the source of suppression of tip-splitting. Figure 6 shows the viscosity $\bar{\mu}_a(We^2 |\nabla p|^2)$ in the fluid external to the bubble, at the final time shown in Fig. 5(b). As expected, we see that the lowest viscosity appears at the ends of the petals. The viscosity increases sharply as one moves away from the tips, and is highest within the fjords, where it is nearly a constant unity (recall that the “zero shear” viscosity is normalized to one). Figure 7(a) shows the viscosity along the bubble interface at several times, including $t=0$, and shows that the viscosity is always lowest in a fairly localized region around the tip.

It is this phenomena that results in the narrowed petals observed from the nonlinear development of the Saffman–Taylor instability: The fluid velocity is locally accentuated by the non-Newtonian effect, which pulls the interface outwards at the tips. Thus, a tip remains a tip, and thereby the conditions for a lower local viscosity are maintained. Of course, this effect is limited by capillarity, which seeks to lower the length to area ratio, and which is also likely related to the production of “side-branches” left behind the advancing tip. As is shown in Sec. VC, one can actually induce the formation of fingers (rather than narrowed petals) by a different choice of viscosity function, even in the open radial geometry.

More information on the production of side-branches is found in Figs. 7(b) and 7(c), which show, respectively, the time evolution of the viscosity and curvature at a petal tip (about $\theta=0$). In the viscosity, we observed an early time behavior characterized by only small changes in absolute value, but having fast, irregular oscillations. We find these oscillations curious, and have no explanation for them, except to note that they persist under refinement in both the space and time resolution. In particular, even if it is not obvious from Fig. 7(b), these small oscillations are smooth: There are approximately 1500 computational time steps and 100 data points presented in this oscillatory region. During this period, the curvature shows little change. These oscillations are followed by a period of monotonic increase in tip viscosity, as the radius of curvature likewise increases (the petal spreads). At somewhere less than $t=3$, the velocity at the petal tips increases relative to the surrounding parts of the interface (a suppression of tip-splitting), which leads to

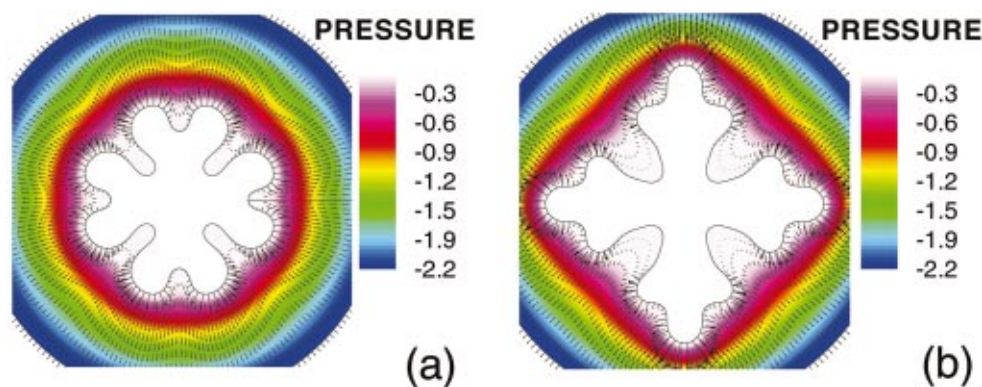


FIG. 8. (Color) The pressure contours and velocity vectors of the driven fluid at the final time: (a) Newtonian fluid; (b) shear-thinning fluid (the parameters are the same as in Fig. 5).

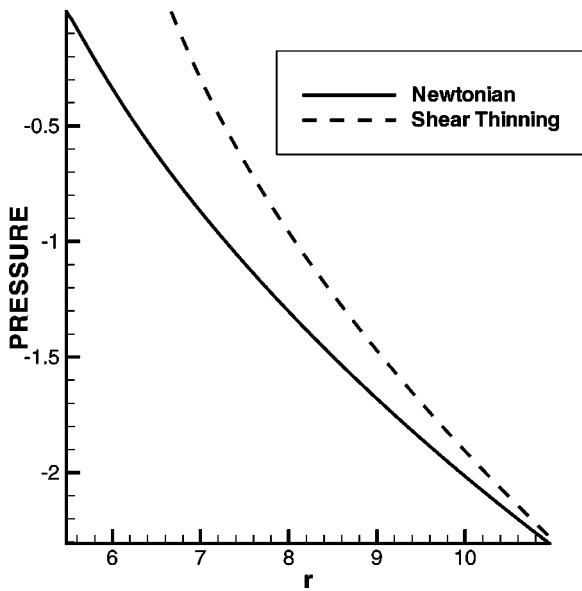


FIG. 9. The pressure in front of the growing tip as a function of radial distance. The data are taken at nondimensional time $t=5.0$ both for Newtonian and shear-thinning case. The parameters are as in Fig. 5.

the shedding of a side-branch, and an ensuing decrease in tip viscosity and radius of curvature. Somewhat later the decrease in tip viscosity slows, the radius of curvature again decreases, but this is followed by yet another shedding of a side-branch, a decrease in the radius of curvature, and a more rapid decrease in tip viscosity.

It is worth re-emphasizing that the side-branches did not originate at the sides of the petal, but rather formed near the tip during the growth of the radius of the curvature, and were left behind the propagating tip. This observation points to the similarity of the pattern formation mechanism in this system to the formation of dendrites in solidification,⁵⁴ even though our system lacks any imposed directionality.

Finally, Fig. 8 shows the pressure distributions at the final times for the Newtonian and non-Newtonian simulations, overlaid by their respective velocity vector fields. We do not observe flattening of the pressure in the shear-thinning fluid, in contrast to what the linear stability analysis in Daccord and Nittmann⁵⁵ and Nittmann, Daccord and Stanley⁵⁶ suggests. Based on this predicted flattening, it was con-

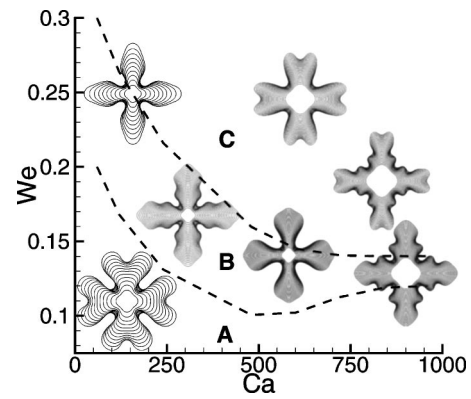


FIG. 10. Phase diagram for pattern formation in the strongly shear-thinning fluid, $\alpha=0.15$, for small values of $We < 0.25$. In **A** one gets wide “Newtonian” petals, in **B** tip-splitting is suppressed, and in **C** narrow (relative to **A**), but tip-splitting petals are observed.

cluded that shear-thinning would not influence considerably the instability structure. Figure 9 shows the pressure in the driven fluid in front of the growing tip versus radial distance, for a Newtonian and a non-Newtonian fluid. The data presented in Fig. 9 are taken at the same time for Newtonian and shear-thinning simulations. The tip of the finger expanding into the shear-thinning fluid has propagated out farther than the tip of the splitting petal growing into the Newtonian fluid. Despite this, the pressure in front of the tips is qualitatively similar in both cases. Away from the tips, the different shapes of the interfaces for the Newtonian and the shear-thinning fluid modify the pressure distribution considerably (Fig. 8).

B. Parametric dependence

Here we explore the role which the three dimensionless parameters, α , Ca and We , play in the bubble evolution.

Figures 10–12 summarize the results of simulations in different regions of this parameter space. (In all cases the initial bubble size is the same. The patterns are enlarged for presentational purposes.) In each of these “phase diagrams,” there is a region (**B**) of the parameter space where splitting of the finger tips is suppressed. Figure 10 illustrates some of the effects of strong shear-thinning ($\alpha=0.15$). For small We we observe “Newtonian” patterns—i.e., widening petals that

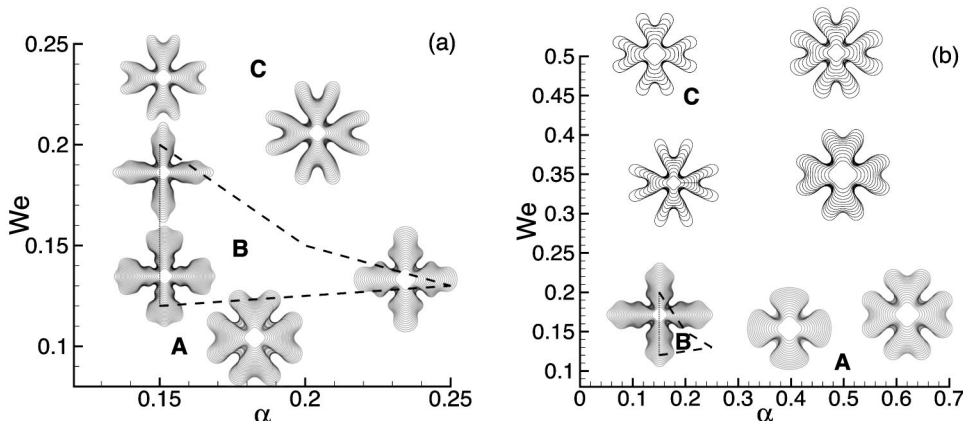


FIG. 11. Phase diagram for fixed $Ca = 240$. Part (a) shows the results for rather strongly shear-thinning fluid, $\alpha < 0.25$, with small values of $We < 0.25$. In **A** one gets wide “Newtonian” fingers, in **B** tip-splitting is suppressed, and in **C** narrow (relative to **A**), but tip-splitting fingers are observed. Part (b) gives the results for a wide range of α and We .

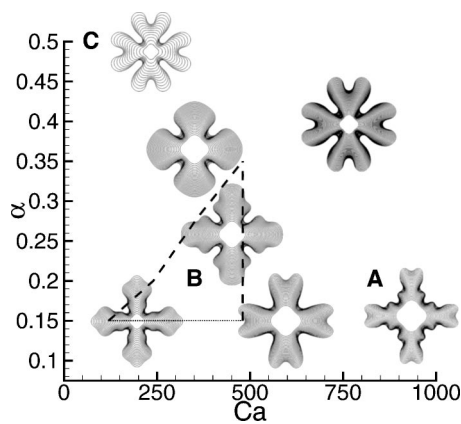


FIG. 12. Phase diagram for fixed $We=0.15$, and for a range of $\alpha < 0.50$, and $Ca < 1000$.

split (region **A**). Increasing We brings us to region **B** where splitting is suppressed. Even higher values of We yield narrow petals, which tip-split (see also Fig. 11).

Note that these general observations agree with what is seen by comparing Figs. 1(a) and 1(b) with Figs. 1(c) and 1(d). For a fixed capillary number, the Weissenberg number decreases by 2.5 in moving from Figs. 1(a) and 1(b) to Figs. 1(c) and 1(d). In this decrease the re-emergence of a more Newtonian pattern is observed (i.e., more tip-splitting).

An increase of Ca leads to the same consequences as for Newtonian fluids: Shorter wavelengths become unstable, which induces tip-splitting (see also Fig. 12). The increase of Ca leads also to a narrowing of region **B**, where tip-splitting is suppressed. In Fig. 10, the size of the window of We for which tip-splitting is suppressed is decreased for $Ca > 500$. Also, increasing Ca shifts this window towards lower We . In an experiment this would mean that if one uses a higher pumping pressure, the fluid should have a shorter relaxation time if nonsplitting tips are to be observed. This effect has, in fact, been observed by Buka, Kertesz and Viscek¹¹ in experiments with nematic liquid crystals,¹¹ where the driving pressure was varied. At low driving pressures, the pattern was Newtonian (corresponding here to small Ca and We —region **A** in Fig. 10). At intermediate driving pressures, the tips did not split (as in region **B**), and finally, high driving pressures (large Ca and We) resulted again in a tip-splitting phase (as in region **C**). These experimental observations agree remarkably well with our results.

Figure 11 shows the phase diagram as α and We are varied while $Ca=240$ is fixed. (We cannot explore the region where $\alpha < 1/9$, where the production of slip layers in the driven fluid might be expected.¹⁸) We focus first on Fig. 11(a), where α and We are rather small, and where the resulting patterns depend quite sensitively on changes of the parameters. As in Fig. 10, a larger We leads to tip-splitting and narrow petals, in contrast to the ones produced for small We . The role of We is to determine which part of the viscosity curve (Fig. 3) governs the viscous response of the fluid. For small values of We , the viscosity in the neighborhood of the tip does not change very much, and the resulting patterns are close to Newtonian (**A**). In Figs. 10–12, the patterns in region (**B**), where nonsplitting fingers are ob-

tained, correspond to the situation where viscosity varies considerably along the interface—this seems to be a necessary condition for the suppression of tip-splitting. At even higher values of We , the viscosity at the tips moves to the lower plateau of the viscosity curve. One might be tempted to explain the observed nonsplitting, narrow, fingers in terms of a local capillary number by using the viscosity at the tips instead of a constant capillary number. However, this would lead to small values of this ‘‘effective’’ Ca , which would predict larger length-scales in region (**C**) than in region (**A**), contrary to our results. The important point here is that there are still very low values of the pressure gradient not only deep in fjords, but also on the finger sides (see Figs. 6 and 8): The flow still sees the steep part of the viscosity curve. Higher viscosity for low pressure gradients further suppresses the motion of the finger sides, leading to the decrease of the resulting length-scales.

Figure 11(b) shows a larger range of α and We of the phase diagram in 11(a). Large values of α and small We yield Newtonian patterns. On the other hand, small α and large We lead to petals which split, but which are narrower than those in region **A**. In this case, the boundary between the regions **A** and **C** is not very sharp; there is a transition region for large values of α and We . An interesting case is $\alpha=0.40$, $We=0.15$, where the effect of shear-thinning is strong enough to prevent splitting (at least at this stage of the growth of the bubble), but not strong enough to produce narrow pointed fingers, such as those formed at smaller values of α . The inspection of Fig. 11 clearly shows that decreasing α leads to the decrease of the resulting length-scales. This effect was observed in experiments with water based muds,¹⁵ which were performed in a channel geometry, where the increase of colloid concentration led to stronger shear-thinning (i.e., a decrease of α), and to the decrease of finger width. Similarly, the recent experiments⁵⁷ with hydroxypropyl methyl cellulose (HPMC) solutions in a radial Hele–Shaw cell showed the decrease of the resulting length-scales with the increase of the concentration of HPMC, which corresponds to stronger shear-thinning.

In Fig. 12, where $We=0.15$, we observe again narrow pointed fingers for small α and Ca (region **B**); narrow, splitting petals for small α , and larger values of Ca (region **A**), and patterns resembling the Newtonian case for larger values of α (region **C**).

Figures 10–12 demonstrate that a strongly shear-thinning fluid is required in order to prevent tip-splitting. We do not observe narrow, nonsplitting fingers for $\alpha > \alpha_{crit} = 0.35$. Also, larger values of Ca typically lead to tip-splitting. Finally, there is a window of We , where tip-splitting is suppressed: This window is shifted towards lower values of We as Ca is increased, becomes narrower for larger values of α , and disappears completely when $\alpha > \alpha_{crit} = 0.35$.

Another effect of tip-splitting is to modify the velocity of the finger tip. Figure 13 shows the tip velocity for two choices of parameters which lead to tip-splitting (Newtonian and $\alpha=0.15$, $We=0.15$, and $Ca=600$), and one choice for which tip-splitting is suppressed ($\alpha=0.15$, $We=0.15$ and $Ca=240$). (Specifically, the tip velocity is calculated at θ

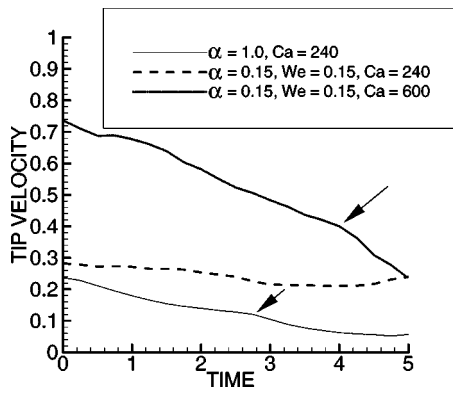


FIG. 13. The velocity of tip propagation, along the x axis. The arrows show the point where curvature of the tip changes sign. A dashed line shows the simulation where fingers do not split.

$=0$, where θ is an azimuthal angle measured from a positive x axis.) The velocity of the splitting petal is continuously decreasing, as the tip of the petal is widening on its route to become a fjord, whereas the velocity of a nonsplitting finger is roughly a constant [the arrows show the points where the curvature of the (former) tip changes sign]. This effect has been noted by Meiburg and Homsy⁵⁸ in a theoretical study of channel flow of Newtonian fluid, where the curvature of the finger tip was held constant artificially. The same study observed also dendritic modes and side-branches.

Remark: There is an intriguing similarity in our results to simulations of Newtonian Hele–Shaw flow with anisotropic boundary conditions,^{59,10} where side-branching was also observed, as well as to local solidification models with anisotropy.⁶⁰ Further, power-law fluids in a rectangular Hele–Shaw cell were recently the subject of a theoretical study (Poiré and Ben Amar^{20,21}). Experiments with foams,¹⁶ where elastic properties might be of importance, and both miscible⁵ and immiscible^{61,57} polymeric liquids, can also produce structures quite similar to ours.

C. Different viscosity models

The form of the developing patterns in Hele–Shaw flow of non-Newtonian fluids is very sensitive to a variation of the parameters which define the viscous response of the fluid. Similar sensitivity has been also widely observed in experiments with polymeric fluids and clays (see, e.g., McCloud and Maher,⁵ Van Damme and Lemaire¹⁵). Consequently, one also expects that the choice of the non-Newtonian viscosity model would influence considerably the response of the driven fluid and pattern formation.

While the use of the viscosity (40) is motivated by the fact that it follows from the well-established JSO model for viscoelastic fluids, it is also of interest to study the patterns resulting from a different viscosity model. Figure 14 shows the evolution of the interface for a fluid with the effective viscosity,

$$\bar{\mu}_\alpha(\text{We}^2|\nabla p|^2) = \frac{1 + \alpha\text{We}^2|\nabla p|^2}{1 + \text{We}^2|\nabla p|^2}, \quad (74)$$

where $1/9 < \alpha < 1$. That is, we define $\bar{\mu}_\alpha(\text{We}^2|\nabla p|^2)$ di-

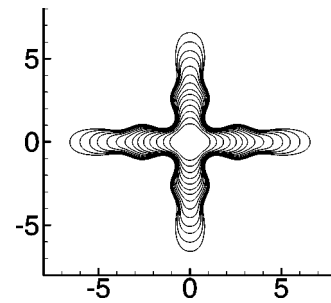


FIG. 14. The snap-shots of the evolving bubble interface for a different viscosity model. Here $\alpha=0.30$, $\text{We}=0.30$, and $\text{Ca}=240$.

rectly, instead of starting with a viscosity function μ and finding the corresponding $\bar{\mu}$ through (43), (46). It is possible to find the physical viscosity μ that yields the effective viscosity in Eq. (74); see Appendix A 4.

In Fig. 14 we see that the growing fingers are much narrower and more elongated than the fingers obtained previously. The oscillatory mode is still present as in Fig. 5(b), even if rather strongly suppressed. We conjecture that the shear-thinning behavior of the driven fluid alone can lead to the suppression of tip-splitting. This feature is independent of the particular model, although the choice of the viscosity model is important if one is interested in the details of the pattern formation.

D. Emerging length-scales

A typical length-scale (l) of patterns which develop in a radial Hele–Shaw flow for Newtonian fluids is determined by the capillary number Ca . For large Ca , linear stability suggests that a length-scale associated with the initial growth of the patterns is given by⁴⁶

$$\lambda_m = \frac{2\pi R}{m_{\text{Newt}}^{\text{max}}} \approx 2\pi R \sqrt{\frac{3}{\text{Ca}}}, \quad (75)$$

where R is the time-dependent radius of the expanding bubble, and we have used the expression for the wavenumber of maximum growth (61). Such a scaling is observed approximately in both simulation and experiment^{32,62,63} for Newtonian flows, and experimentally for non-Newtonian flows.^{56,55} We look into our simulation results for a similar length scaling in shear-thinning liquids.

Figure 15 shows the length-scales emerging from the simulation of a strongly shear-thinning fluid, as well as the result of linear stability analysis and a fit of the form $A \text{Ca}^{-1/2}$. Here the length-scale was approximated by measuring the radius of curvature at the tip of a growing finger. As we have shown, the curvature can oscillate at the tip and so we plot a representative value where the error bars show the size of the fluctuations. Note that this length-scale is measured in the strongly nonlinear regime, where the results of linear theory would not be expected to apply. The linear stability result is obtained by assuming that the radius of the bubble is equal to its initial size, so $R=1$ in (75). In the apparent form of its decrease with Ca , the results of linear stability for the shear-thinning liquid is consistent with the fit. And while it is unclear that the simulational length-scale

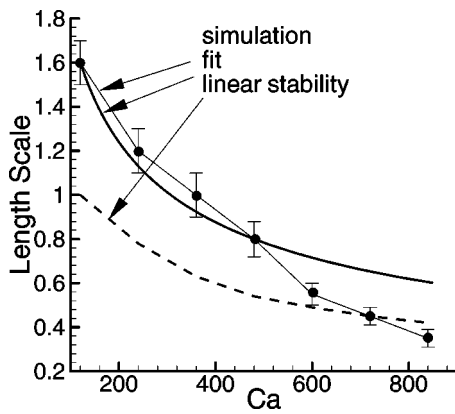


FIG. 15. Capillary number dependence of the length-scale (l) of the most unstable modes following from linear stability (dashed), emergent length-scales from the simulations (dots) and the fit of the form $A Ca^{-1/2}$ (solid), where A is taken from the first data point. Here $\alpha=0.15$ and $We=0.15$.

behaves as $Ca^{-1/2}$, there is a reasonable agreement in magnitude between the simulations and the result of linear theory.

In experiments using a shear-thinning polymeric solution being displaced by water,^{56,55} emerging length-scales have been measured as the gap width b is varied, apparently while holding fixed the characteristic velocity \dot{R}_0 . These results suggest that the length-scale scales linearly with b . For Newtonian fluids this observation confirms the result of linear stability, since $Ca \sim 1/b^2$ if the characteristic velocity is fixed independently of b . However, the flow also depends up the Weissenberg number, We , which is itself a function of b . So, one should modify both Ca and We accordingly, in order to obtain a realistic comparison with experimental results. These resulting length-scales measured in this way are given in Fig. 16. Since our simulational results (and the experimental observations^{56,55}) suffer from relatively large uncertainty, we cannot conclude from this that scaling $l \sim b$ is satisfied. Still there is a good qualitative agreement of the simulations and the experimental results.

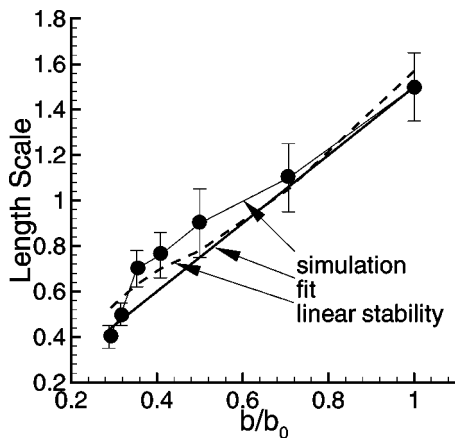


FIG. 16. The dependence of the length-scale (l) on plate separation b . Here b_0 is the plate separation which gives $Ca=240$ and $We=0.15$ at $t=0$. Linear stability results (dashed), simulation results (dots) and fit $l \sim b$ (solid) are shown ($\alpha=0.15$). The constant k required for fitting line $L=kb$ is determined from the data point $b=b_0$.

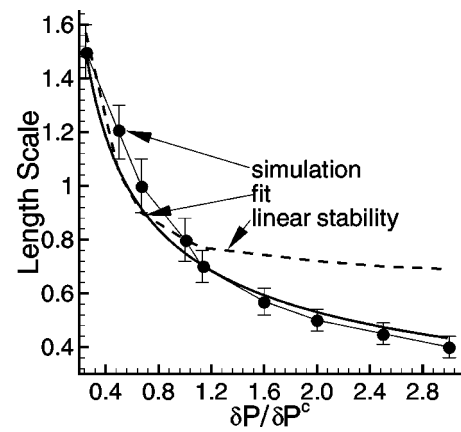


FIG. 17. The dependence of the length-scales on driving pressure δP . Here δP^c is the driving pressure which gives $Ca=240$ and $We=0.15$. Linear stability results (dashed), simulation results (dots) and fit $l \sim k(\delta P / \delta P^c)^{-1/2}$ (solid) are shown. The constant k is determined from the data point $\delta P = \delta P^c$.

The driving pressure is another control parameter whose influence on emerging length-scales can be explored. In experiments [air displacing water based muds¹⁵ and HPMC (polymeric) solutions^{61,57}] increasing the driving pressure typically decreases the observed length-scales.^{15,61,57} However, these experimental data are not very precise in expressing the length-scale dependence upon the driving pressure. Figure 17 compares the length-scales obtained from our simulations to the results of linear stability, and to a fitting function of the form $l \sim 1/\sqrt{\delta P}$, where δP is the driving pressure. The motivation for this particular fit arises from analogy with Newtonian fluids where $l \sim 1/\sqrt{Ca}$, and $Ca \sim \delta P$ (see also Fig 15). Here we observe that linear stability theory and simulational results agree rather well at smaller driving pressures. For larger values of δP , the length-scales resulting from linear stability analysis saturate to a constant, while the results of the simulations fit $l \sim 1/\sqrt{\delta P}$ very closely. We hope to verify this prediction experimentally.⁶⁴

Figure 18 shows the possible source of emerging length-scales for shear-thinning fluids. This figure presents the variation of viscosity in radial direction in front of the tip $\mu(r)$, the viscosity in the fluid adjacent to the interface $\mu(S)$

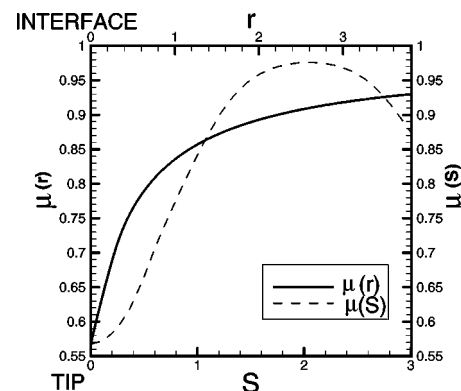


FIG. 18. The curvature of the interface $\kappa(S)$, viscosity in the fluid along the interface $\mu(S)$ and viscosity in the radial direction $\mu(r)$ are shown. Here r is radial distance from the tip and S is the arc-length measured from the tip.

and the curvature $\kappa(S)$ along the interface, where r is the radial distance from the tip and S is the arc-length along the interface, measured from the tip. The data are taken from the last time presented in Fig. 5. It is intriguing that the length-scales on which each of these quantities vary substantially are comparable (of course, the curvature of the tip gives approximately the length-scale on which curvature along the interface changes sign). In particular, we observe that the variation of viscosity in the radial direction compares well with the variation of viscosity along the interface (Fig. 6). We conjecture that the length-scale associated with the viscosity variation in a driven fluid relates closely to the length-scale of emerging patterns.

VI. CONCLUSION

In this paper we have shown that, under certain assumptions, flow in a Hele–Shaw cell of a complex viscoelastic fluid simplifies to that of a generalized Newtonian fluid. Full numerical simulations of the two phase (liquid/gas) flow show that shear-thinning behavior of the driven fluid modifies significantly the morphology of the patterns, relative to those for Newtonian liquids, by suppressing tip-splitting. This can lead to structures of dendritic appearance resembling those occurring in quasistatic solidification. These results are consistent with available experimental results. Further, we provide morphological phase diagrams that show the flow and fluid parameters required to suppress tip-splitting. Lastly, the varying of length-scales emerging from our simulations, as parameters are changed, is in reasonable agreement with those observed in experiments. In particular, we observe in our simulations that the typical length-scale of the patterns scales with driving pressure as $l \sim P_0^{-1/2}$ —this prediction is still to be verified experimentally.

We have ignored in this work several potentially important aspects of these flows, that preclude us from having a fuller understanding of these problems. First, better comprehension is needed of the flows close to the interface. Corrections to the simple Laplace–Young boundary condition have been derived for Newtonian fluids (see Homsy⁶⁵ and the references therein) that account for the presence of a meniscus and of films wetted to the cell plates. This has been done to a lesser degree for non-Newtonian fluids (Ro and Homsy^{65,37}). An elastic response is also likely to be important in the neighborhood of the meniscus, and an improved understanding of the boundary flows would lead to a more quantitative understanding of the coil–stretch transition.³¹ Second, in our scaling we do not allow for an elastic response in the bulk fluid, that is, we look at flow only at order one Weissenberg number. To consider higher Weissenberg numbers would apparently require solving fully time-dependent PDEs for the extra stress in the bulk fluid. It would be of interest to find some scaling of the equations that would allow this to be done in a tractable way. Lastly, by our construction of the effective viscosities, we have certainly not allowed for the possibility of slip-layer formation (see Kondic, Palfy-Muhoray and Shelley¹⁸ and the references therein). Though the origin of wall slip is still controversial,²³ the JSO equations do formally allow for

shearing flows with slip layers though having a nonmonotonic stress/rate-of-strain relation (for $\alpha < 1/9$).

Nonetheless, given that our present (relatively simple) approximation seems to capture many of the salient features of shear-thinning flows—in particular the suppression of tip-splitting—there are some fundamental questions to be answered. A central one is understanding at a detailed level how this system, without any explicit anisotropy, forms fingering structures so reminiscent of directional solidification. Obviously, an effective anisotropy is being created nonlinearly by the shear-thinning, and is intimately related to the suppression of tip-splitting. Understanding this will require mathematical analyses combined with refined experiments and accurate numerical simulation.

The analysis of Poiré and Ben Amar^{20,21} on finger selection in weakly shear-thinning, power law fluids is a first effort in this direction. Another mathematical approach that could be fruitful to expand upon follows from the work of Miranda and Widom⁶⁶ on tip-splitting in Newtonian flows. They execute a slightly nonlinear analysis to understand how mode coupling dynamics leads to tip-splitting. Perhaps for a shear-thinning flow such an approach would show how mode coupling instead suppresses tip-splitting. Improved numerical approaches to evolving the interface efficiently, and especially accurately, will also allow a calculation of the patterns over a longer time, as has been done for Newtonian flows,⁶ to see whether the structures we have found here persist, and how the patterns are characterized. It is also important to understand how the patterns observed depend on the details of the particular viscosity model. In this vein, given the gross similarity of patterns observed in liquid crystals^{11,12} and foams¹⁶ to those seen in shear-thinning liquids, one might expect to find modified Darcy’s laws that are similar to those found here.

ACKNOWLEDGMENTS

We would like to thank Bastiaan Braams, Jens Eggers, and David Muraki for useful conversations. This work was supported in part by National Science Foundation Grants No. DMS-9404554 and No. DMS-9396403 (M.J.S., P.F.), AL-COM Grant No. DMR89-20147 and AFOSR MURI Grant No. F4962-97-1-0014 (P.P.-M.), Department of Energy (DOE) Grant No. DE-FG02-88ER25053 (M.J.S., P.F., L.K.), and NJIT Grant No. 421210 (L.K.). A part of this work was performed under the auspices of the U.S. Department of Energy by University of California Lawrence Livermore National Laboratory under Contract No. W-7405-Eng-48.

APPENDIX: PROPERTIES OF THE EFFECTIVE VISCOSITY $\bar{\mu}$

Our theory builds upon two basic assumptions: (i) The transformation defined by Eqs. (43),(46), from μ to $\bar{\mu}$ and $\bar{\mu}$ is well-defined, and (ii) the nonlinear BVP (51) has a solution. We show here that a reasonable condition that guarantees the existence of the effective viscosity $\bar{\mu}$ is also sufficient for Eq. (51) to be solvable. Further, we show in Appendix A 2 that the monotonicity of μ is inherited by $\bar{\mu}$

and $\bar{\mu}$, and in Appendix A 4 that given a $\bar{\mu}$, we can find the corresponding μ , under suitable restrictions. A closed form expression for $\bar{\mu}$ is given in Sec. A 5.

1. Invertibility

The following theorem gives a sufficient condition for the inverse viscosity $\bar{\mu}$ of μ to be well-defined.

Proposition 1: *Let $\mu(s^2) > 0$ for all s , $f(s) = \mu(s^2)s$ be continuously differentiable, and*

$$0 < C_0 \leq \mu(s^2) + 2s^2 \mu'(s^2) \leq C_1 < \infty, \tag{A1}$$

for some constants C_0, C_1 . Then the inverse viscosity $\bar{\mu}$ can be defined by (43), and it satisfies

$$0 < C'_0 \leq \frac{\bar{\mu}(z^2) - 2z^2 \bar{\mu}'(z^2)}{\bar{\mu}^2(z^2)} \leq C'_1 < \infty. \tag{A2}$$

Proof: The function f is strictly increasing, so its inverse function $g = f^{-1}$ exists. Since $g'(f(s)) = 1/f'(s)$, and $0 < C_0 \leq f'(s^2) \leq C_1 < \infty$ by (A1), we obtain $0 < 1/C_0 \leq g'(z^2) \leq 1/C_1$. At $z = 0$ we have $g(0) = 0$,

$$\bar{\mu}(0) = \lim_{z \rightarrow 0} \frac{z}{g(z)} = \frac{1}{g'(0)} = f'(0) = \mu(0),$$

and $g(z) > 0$ for $z \neq 0$.

The inverse viscosity can now be defined as $\bar{\mu}(z^2) = z/g(z)$ for all z . Equation (A2) follows by noting $g'(z) = (\bar{\mu}(z^2) - 2z^2 \bar{\mu}'(z^2))/\bar{\mu}^2(z^2)$.

This motivates the following definitions.

Definition 2: *A function $\mu: \mathbb{R} \rightarrow \mathbb{R}$ is called a viscosity (function) if $\mu \geq C > 0$ for a constant C , and $f(s) = \mu(s^2)s$ is continuously differentiable.*

The viscosity function is called monotonic if μ is monotonically increasing or decreasing. A viscosity function is called bounded if $0 < C \leq \mu \leq C' < \infty$.

Definition 3: *A viscosity function μ is called invertible if*

$$0 \leq C_0 \leq \mu(s^2) + 2s^2 \mu'(s^2) \leq C_1 < \infty,$$

for some constants C_0, C_1 .

We will not consider viscosity functions that are not invertible in the sense of Definition 3 in this work, although they are certainly interesting.²³ The definitions given above are natural, as one sees from the solvability conditions discussed in Sec. A 3.

2. Monotonicity and derivatives of the viscosities

The inverse viscosity $\bar{\mu}$ and the effective viscosity $\bar{\mu}$ inherit the monotonicity of the original viscosity function μ .

Proposition 4: *Let μ be a monotonic, invertible viscosity function. Then $\mu', \bar{\mu}'$ and $\bar{\mu}'$ have the same sign.*

Proof: By a direct calculation. First consider $\bar{\mu}$, and note that

$$\bar{\mu}(z^2) = \mu\left(\frac{z^2}{\bar{\mu}(z^2)}\right), \tag{A3}$$

for any z by Eq. (43). Taking a z -derivative of Eq. (A3) together with Proposition 1 shows that μ' and $\bar{\mu}'$ have the same sign.

To show $\bar{\mu}'$ and $\bar{\mu}'$ have the same sign, differentiate the definition of $\bar{\mu}$. Together with the first part this implies that $\mu, \bar{\mu}$ and $\bar{\mu}$ have the same sign.

3. Solvability of the BVP

In this section, we find conditions on μ that are sufficient for

$$\nabla \cdot \left(\frac{\nabla p}{\bar{\mu}(|\nabla p|^2)} \right) = 0, \text{ in } \Omega, \quad p = f, \text{ on } \partial\Omega, \tag{A4}$$

to have a unique classical solution. Here Ω is a connected, bounded domain in the plane, f is a given and $\bar{\mu}$ is an effective viscosity.

To avoid technicalities, we assume the boundary of the domain and all functions to be sufficiently smooth when the underlying theorems require, e.g., Holder-continuity. (See Gilbarg and Trudinger⁶⁷ for details.) Continuous differentiability is sufficient for most purposes here. Classical solutions of (A4) are at least twice continuously differentiable. Note that the results give sufficient conditions, and one could certainly look for more general results.

The main result of this subsection is given by the following.

Proposition 5: *Let the effective viscosity $\bar{\mu}$ correspond to a viscosity function μ that satisfies*

$$0 < C_0 \leq \mu(s^2) + 2s^2 \mu'(s^2) \leq C_1 < \infty, \tag{A5}$$

for some constants C_0, C_1 . Then the nonlinear BVP (A4) has a unique classical solution.

The essence of this proposition lies within two facts: (1) The solvability of Eq. (A4) is expressed in terms of the physical viscosity μ , and (2) the solvability is guaranteed by the same condition as the invertibility of the viscosity. The proof amounts to showing that (A4) satisfies the conditions of a classical result (Lemma 6). We have collected the required calculations in a sequence of lemmas.

Equation (A4) can be written in an equivalent, nonconservative form as

$$a(p_x, p_y) p_{xx} + 2b(p_x, p_y) p_{xy} + c(p_x, p_y) p_{yy} = 0, \tag{A6}$$

where

$$a = \frac{\bar{\mu} - 2p_x^2 \bar{\mu}'}{\bar{\mu}^2}, \quad b = -\frac{2p_x p_y \bar{\mu}'}{\bar{\mu}^2},$$

and

$$c = \frac{\bar{\mu} - 2p_y^2 \bar{\mu}'}{\bar{\mu}^2}.$$

We write $\bar{\mu} = \bar{\mu}(|\nabla p|^2)$ and $\bar{\mu}' = \bar{\mu}'(|\nabla p|^2)$ for clarity.

Lemma 6: *Assume the coefficients a, b, c are smooth, and the eigenvalues λ, Λ of the coefficient matrix,*

$$\begin{pmatrix} a & b \\ b & c \end{pmatrix}, \tag{A7}$$

are strictly positive and satisfy $1 \leq \Lambda/\lambda < \gamma < \infty$ for some constant γ . Then (A4) has a unique classical solution.

Proof: Gilbarg and Trudinger,⁶⁷ Theorem 12.5.

Lemma 7: The coefficient matrix (A7) has the eigenvalues

$$\lambda_{\pm} = \frac{\bar{\mu} - |\nabla p|^2 \bar{\mu}'}{\bar{\mu}^2} \pm \left| \frac{\bar{\mu}' |\nabla p|^2}{\bar{\mu}^2} \right|.$$

Proof: By a direct calculation.

Lemma 8: Let a viscosity function μ be bounded and invertible. Then

$$0 < D_0 \leq \frac{\bar{\mu} - |\nabla p|^2 \bar{\mu}'}{\bar{\mu}} \leq D_1 < \infty,$$

for some constants D_0, D_1 .

We defer the proof of this technical Lemma after the following.

Proof of Proposition 5: We will show that the assumptions of the Proposition imply those of Lemma 6. First, consider a shear thinning fluid with $\mu'(s^2) \leq 0$. Then by Lemma 7 the eigenvalues of the coefficient matrix are

$$\lambda = \frac{1}{\bar{\mu}}, \quad \Lambda = \frac{\bar{\mu} - 2|\nabla p|^2 \bar{\mu}'}{\bar{\mu}^2},$$

and we have $0 < \lambda < \Lambda$. The ratio of these satisfies

$$1 \leq \frac{\Lambda}{\lambda} = \frac{\bar{\mu} - |\nabla p|^2 \bar{\mu}'}{\bar{\mu}} \leq \gamma < \infty,$$

where the lower bound follows from shear thinning, and the upper bound follows from Lemma 8 with γ a constant. Lemma 6 can now be applied. The case of a shear thickening viscosity, $\mu'(s^2) > 0$, follows similarly with λ and Λ switched.

Proof of Lemma 8: Denote $\xi = |\nabla p|$, and note that

$$\begin{aligned} \bar{\mu} \frac{d}{d\xi} \left(\frac{\xi}{\bar{\mu}(\xi^2)} \right) &= \frac{\bar{\mu} - 2\xi^2 \bar{\mu}'}{\bar{\mu}} \\ &= 12\bar{\mu} \int_{-1/2}^{1/2} \left[\frac{\bar{\mu}(\xi^2 z^2) - 2\xi^2 z^2 \bar{\mu}'(\xi^2 z^2)}{\bar{\mu}^2(\xi^2 z^2)} \right] z^2 dz. \end{aligned} \tag{A8}$$

Since μ is bounded and invertible, the term in the square brackets is strictly positive and bounded by Proposition 1. If μ is invertible then the corresponding effective viscosity $\bar{\mu}$ is bounded and strictly positive, as one sees from its definition (46). It follows that

$$0 < \frac{\bar{\mu}_{\min}}{C_1} \leq \frac{\bar{\mu} - 2\xi^2 \bar{\mu}'}{\bar{\mu}} \leq \frac{\bar{\mu}_{\max}}{C_0} < \infty,$$

where $\bar{\mu}_{\min}, \bar{\mu}_{\max}$ is a lower and upper bound of $\bar{\mu}$, respectively.

4. Inverting the transformation

The transformation $\mu \rightarrow \bar{\mu} \rightarrow \bar{\mu}$ can be inverted, that is, given a suitable $\bar{\mu}$ it is possible to find the corresponding $\bar{\mu}$, and thereby μ , in Eq. (46).

Proposition 9: Let $\bar{\mu}$ satisfy

- (i) $0 < C_0 \leq \bar{\mu}(\xi^2) - 2\xi^2 \bar{\mu}'(\xi^2) \leq C_1 < \infty$, for all ξ ;
- (ii) $0 < C_2 \leq \bar{\mu}(\xi^2) \leq C_3 < \infty$,

where C_0, \dots, C_3 are constants. Then the inverse viscosity,

$$\bar{\mu}(\xi^2) = \frac{\bar{\mu}^2(4\xi^2)}{\bar{\mu}(4\xi^2) - \frac{2}{3} \cdot 4\xi^2 \bar{\mu}'(4\xi^2)}, \tag{A9}$$

satisfies Eqs. (43), (46).

Proof: It follows from Eq. (46) by taking a derivative and integration by parts. Then

$$\begin{aligned} \frac{-2\xi \bar{\mu}'(\xi^2)}{\bar{\mu}^2(\xi^2)} &= 24 \left[\frac{z^3}{\xi \bar{\mu}(\xi^2 z^2)} \right]_{z=0}^{1/2} - 24 \int_0^{1/2} \frac{3z^2 dz}{\xi \bar{\mu}(\xi^2 z^2)} \\ &= \frac{3}{\xi \bar{\mu}(\xi^2/4)} - \frac{3}{\xi \bar{\mu}(\xi^2)}, \end{aligned} \tag{A10}$$

so that $\bar{\mu}$ can be solved as a function of $\bar{\mu}$ to get Eq. (A9).

The expression (A9) is valid as long as the denominator is not zero. This is clear for shear-thinning fluids, for which $\bar{\mu}' < 0$ by Sec. A 2. In fact, Eq. (A9) holds for all uniquely invertible viscosity functions.

Let $\bar{\mu}'(s^2) > 0$ and consider the denominator of Eq. (A9). It can be bounded from below by using the definition of $\bar{\mu}$ and Eq. (A10) to yield

$$\begin{aligned} &\bar{\mu}(4\xi^2) - \frac{2}{3} \cdot 4\xi^2 \bar{\mu}'(4\xi^2) \\ &> \bar{\mu}(4\xi^2) - 2(4\xi^2) \bar{\mu}'(4\xi^2) \\ &= 12\bar{\mu}^2(4\xi^2) \int_{-1/2}^{1/2} z^2 \frac{\bar{\mu}(4\xi^2 z^2) - 2(4\xi^2 z^2) \bar{\mu}'(4\xi^2 z^2)}{\bar{\mu}^2(4\xi^2 z^2)} dz \\ &> 0, \end{aligned}$$

for any ξ , since the integrand is strictly positive if $\bar{\mu}$ satisfies the invertibility condition (A2).

Example: Instead of using the effective viscosity corresponding to $\mu(s^2) = (1 + \alpha s^2)/(1 + s^2)$, one could consider more general effective viscosities. A particularly interesting choice is

$$\bar{\mu}(s^2) = \frac{1 + \alpha s^2}{1 + s^2}, \tag{A11}$$

which is also discussed in Sec. V C. Note that $\bar{\mu}$ is specified directly, instead of going through the transformation (46).

Using the inversion formula (A9), we can find the viscosity function μ corresponding to the effective viscosity function of Eq. (A11). This requires the invertibility conditions for $\bar{\mu}$ to hold, so $\alpha > 1/9$.

Equation (A9) gives now

$$\bar{\mu}(z^2) = \frac{3(1 + 4\alpha z^2)^2}{3 + 4(5 + \alpha)z^2 + 48\alpha z^4}.$$

An analytical expression for the corresponding μ seems unattainable. However, we can still plot the corresponding μ using the following simple observation.

First, define $s = s(z)$ in Eq. (43). Then one has $\mu(s(z)^2) = \bar{\mu}(z^2)$. This allows us to plot $(s, \mu(s^2))$ as $(s(z), \bar{\mu}(z^2))$, where $s(z) = z/\bar{\mu}(z^2)$. Figure 19 compares the effective viscosity given by Eq. (A11) to those obtained from JSO, and the corresponding physical viscosities.

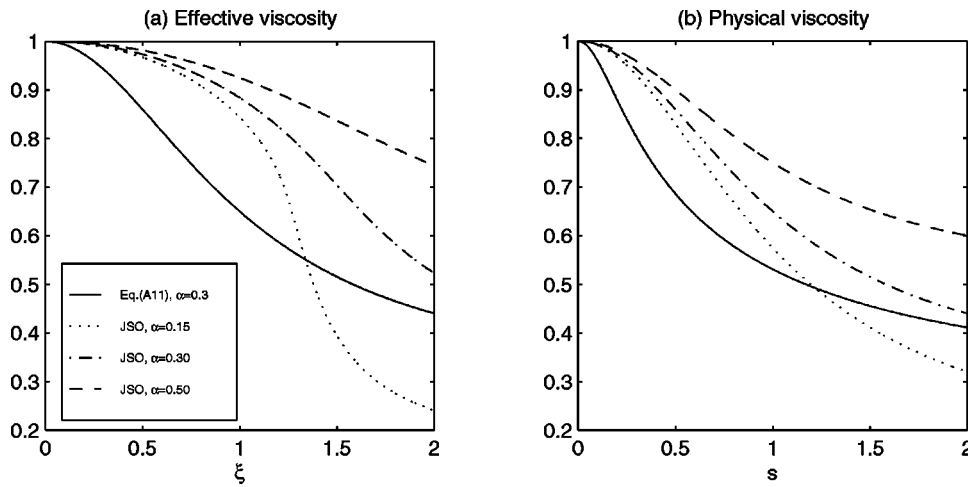


FIG. 19. Comparing the effective viscosity $\bar{\mu}(\xi) = (1 + \alpha\xi^2)/(1 + \xi^2)$ to those obtained from JSO. Varying α in JSO does not significantly change the slope of the effective viscosity [see (a)], or the physical viscosity [see (b)], at small shear-rates. The shear-rate dependency of the effective viscosity in Eq. (A11) at small shear rates is much stronger than that in JSO.

5. Explicit $\bar{\mu}$ for JSO

The gap-averaging (46) of the viscosity requires the integration of the inverted viscosity $\bar{\mu}$. For completeness, we show here how to find a closed form expression for $\bar{\mu}$, which is defined as

$$\frac{1}{12\bar{\mu}(\xi^2)} = \int_{-1/2}^{1/2} \frac{z^2 dz}{\bar{\mu}(\xi^2 z^2)}. \tag{A12}$$

Now, let $z(s) = \mu(s^2)s$ and note that $s = z(s)/\bar{\mu}(z(s)^2)$, so that especially $\bar{\mu}(z(s)^2) = \mu(s^2)$ holds. By changing the variable of integration to s and integration by parts we obtain

$$\frac{1}{12\bar{\mu}(\xi^2)} = \frac{2}{\xi^3} \int_0^{\xi/2} \frac{(\mu(s^2)s)^2}{\mu(s^2)} \frac{d}{ds}(\mu(s^2)s) ds, \tag{A13}$$

$$= \frac{1}{\xi^3} \left\{ \chi^3 \mu(\chi^2)^2 - \int_0^\chi \left(\frac{1 + \alpha s^2}{1 + s^2} \right)^2 ds \right\}, \tag{A14}$$

where $\chi = (\xi/2)/\mu(\xi^2/4)$, and we specialized to JSO. (The same approach works for other viscosity functions.) The final result for the gap-averaged viscosity is given by

$$\bar{\mu}(\xi^2) = \frac{\xi^3}{24} \cdot \left[2\alpha(\alpha-1)\chi + \left(\mu^2(\chi^2) - \frac{\alpha^2}{3} \right) \chi^3 - \frac{C}{2} \arctan \chi + \frac{1}{2}(\alpha-1)^2 \frac{\chi}{1+\chi^2} \right]^{-1}, \tag{A15}$$

where $C = (5\alpha^2 - 6\alpha + 1)$,

$$\bar{\mu}(z^2) = \frac{1}{3} + q^{1/3} + \frac{1 - 3z^2}{9q^{1/3}},$$

and

$$q = \frac{2 + 9(3\alpha - 1)z^2}{54} + \left(\frac{z^2}{108} (4z^4 + (3(3\alpha - 1)^2 - 4)z^2 + 4\alpha) \right)^{1/2}.$$

Equation (A15), although exact, is numerically ill-conditioned for small arguments ξ , in which case one can use the approximation

$$\bar{\mu}(\xi^2) = 1 - \frac{3(1-\alpha)}{20} \xi^2 + O(\xi^4).$$

¹C. A. Hieber, in *Injection and Compression Molding Fundamentals*, edited by A. I. Isayev (Marcel Dekker, New York, 1987).
²C. Z. Van Doorn, “Dynamic behavior of twisted nematic liquid-crystal layers in switched fields.” *J. Appl. Phys.* **46**, 3738 (1975).
³J. S. Langer, in *Statistical Physics*, edited by H. E. Stanley (North-Holland, Amsterdam, 1986).
⁴J. O’M. Bockris and A. K. N. Reddy, *Modern Electrochemistry* (Plenum, New York, 1970).
⁵K. V. McCloud and J. V. Maher, “Experimental perturbations to Saffman–Taylor flow,” *Phys. Rep.* **260**, 139 (1995).
⁶T. Hou, J. Lowengrub, and M. J. Shelley, “Removing the stiffness from interfacial flow with surface-tension,” *J. Comput. Phys.* **114**, 312 (1994).
⁷T. C. Halsey and M. Leibig, “Theory of branched growth,” *Phys. Rev. A* **46**, 7793 (1992).
⁸E. Ben-Jacob, R. Godbey, N. D. Goldenfeld, J. Koplik, H. Levine, T. Mueller, and L. M. Sander, “Experimental demonstration of the role of anisotropy in interfacial pattern formation,” *Phys. Rev. Lett.* **55**, 1315 (1985).
⁹Y. Couder, N. Gerard, and M. Rabaud, “Narrow fingers in the Saffman–Taylor instability,” *Phys. Rev. A* **34**, 5175 (1986).
¹⁰R. Almgren, W. S. Dai, and V. Hakim, “Scaling behavior in anisotropic Hele–Shaw flow,” *Phys. Rev. Lett.* **71**, 3461 (1993).
¹¹A. Buka, J. Kertesz, and T. Viscek, “Transitions of viscous fingering patterns in nematic liquid-crystals,” *Nature (London)* **323**, 424 (1986).
¹²A. Buka, P. Palfy-Muhoray, and Z. Racz, “Viscous fingering in liquid crystals,” *Phys. Rev. A* **36**, 3984 (1987).
¹³H. Zhao and J. V. Maher, “Viscoelastic effects in patterns between miscible liquids,” *Phys. Rev. A* **45**, R8328 (1992).
¹⁴H. Zhao and J. V. Maher, “Associating-polymer effects in a Hele–Shaw experiment,” *Phys. Rev. E* **47**, 4278 (1993).
¹⁵H. Van Damme and E. Lemaire, “Non-Newtonian fingering and viscoelastic fracturing,” in *Disorder and Fracture*, edited by J. C. Charmet, S. Roux, and E. Guyon (Plenum, New York, 1990), p. 83.
¹⁶S. S. Park and D. J. Durian, “Viscous and elastic fingering instabilities in foam,” *Phys. Rev. Lett.* **72**, 3347 (1994).
¹⁷M. W. Johnson, Jr. and D. Segalman, “A model for viscoelastic fluid behaviour which allows non-affine deformation,” *J. Non-Newtonian Fluid Mech.* **2**, 255 (1977).
¹⁸L. Kondic, P. Palfy-Muhoray, and M. J. Shelley, “Models of non-Newtonian Hele–Shaw flow,” *Phys. Rev. E* **54**, 4536 (1996).
¹⁹L. Kondic, M. J. Shelley, and P. Palfy-Muhoray, “Non-Newtonian Hele–Shaw flow and the Saffman–Taylor instability,” *Phys. Rev. Lett.* **80**, 1433 (1998).
²⁰E. C. Poiré and M. Ben Amar, “Finger behavior of a shear thinning fluid in a Hele–Shaw cell,” *Phys. Rev. Lett.* **81**, 2048 (1998).
²¹M. Ben Amar and E. C. Poiré, “Pushing a non-Newtonian fluid in a Hele–Shaw cell: From fingers to needles,” *Phys. Fluids* **11**, 1757 (1999).

- ²²A. Lindner, D. Bonn, and J. Meunier, "Viscous fingering in a shear-thinning fluid," *Phys. Fluids* **12**, 256 (2000).
- ²³D. S. Malkus, J. A. Nohel, and B. J. Plohr, "Analysis of new phenomena in shear flow of non-Newtonian fluids," *SIAM (Soc. Ind. Appl. Math.) J. Appl. Math.* **51**, 899 (1991).
- ²⁴R. G. Larson, *Constitutive Equations for Polymer Melts and Solutions* (Butterworth, Stoneham, MA, 1988).
- ²⁵M. Keentok, A. G. Georgescu, A. A. Sherwood, and R. I. Tanner, "The measurement of the second normal stress difference for some polymeric solutions," *J. Non-Newtonian Fluid Mech.* **6**, 303 (1980).
- ²⁶R. B. Bird, R. C. Armstrong, and O. Hassager, *Dynamics of Polymeric Liquids* (Wiley, New York, 1987).
- ²⁷D. Bonn, H. Kellay, M. Ben Amar, and J. Meunier, "Viscous finger widening with surfactants and polymers," *Phys. Rev. Lett.* **75**, 2132 (1995).
- ²⁸H. Bonn, D. Kellay, M. Braunlich, M. Ben Amar, and J. Meunier, "Viscous fingering in complex fluids," *Physica A* **220**, 60 (1995).
- ²⁹C.-W. Park and G. M. Homsy, "Two-phase displacement in Hele-Shaw cells: Theory," *J. Fluid Mech.* **139**, 291 (1984).
- ³⁰D. A. Reinelt and P. G. Saffman, "The penetration of a finger into a viscous fluid in a channel and tube," *SIAM (Soc. Ind. Appl. Math.) J. Sci. Stat. Comput.* **6**, 542 (1985).
- ³¹D. E. Smith, X. Z. Wu, A. Libchaber, E. Moses, and T. Witten, "Viscous finger narrowing at the coil-stretch transition in a dilute polymer solution," *Phys. Rev. A* **45**, 2165 (1992).
- ³²P. Tabeling, G. Zocchi, and A. Libchaber, "An experimental study of the Saffman-Taylor instability," *J. Fluid Mech.* **177**, 67 (1987).
- ³³F. P. Bretherton, "The motion of long bubbles in tubes," *J. Fluid Mech.* **10**, 166 (1961).
- ³⁴D. A. Reinelt, "Interfacial conditions for two-phase displacement in Hele-Shaw cells," *J. Fluid Mech.* **183**, 219 (1987).
- ³⁵D. A. Reinelt, "The effect of thin film variations and transverse curvature on the shape of fingers in a Hele-Shaw cell," *J. Fluid Mech.* **285**, 303 (1995).
- ³⁶J. W. McLean and P. G. Saffman, "The effect of surface-tension on the shape of fingers in a Hele-Shaw cell," *J. Fluid Mech.* **102**, 455 (1981).
- ³⁷J. Ro and G. M. Homsy, "Viscoelastic free surface flows: Thin film hydrodynamics of Hele-Shaw and dip coating flows," *J. Non-Newtonian Fluid Mech.* **57**, 203 (1995).
- ³⁸S. D. R. Wilson, "The Taylor-Saffman problem for a non-Newtonian liquid," *J. Fluid Mech.* **220**, 413 (1990).
- ³⁹V. Gauri and K. W. Koelling, "Gas-assisted displacement of viscoelastic fluids: Flow dynamics at the bubble front," *J. Non-Newtonian Fluid Mech.* **83**, 183 (1999).
- ⁴⁰P. C. Huzyak and K. W. Koelling, "The penetration of a long bubble through a viscoelastic fluid in a tube," *J. Non-Newtonian Fluid Mech.* **71**, 73 (1997).
- ⁴¹G. I. Taylor, "Motion of long bubbles in a tube," *J. Fluid Mech.* **10**, 161 (1960).
- ⁴²P. G. De Gennes, "Coil-stretch transition of dilute flexible polymers under ultrahigh velocity gradients," *J. Chem. Phys.* **60**, 5030 (1974).
- ⁴³P. Fast, "Dynamics of interfaces in non-Newtonian Hele-Shaw flow," Ph.D. thesis, Courant Institute, New York University, 1999.
- ⁴⁴L. D. Landau and E. M. Lifshitz, *Fluid Mechanics*, 2nd ed. (Pergamon, New York, 1987).
- ⁴⁵P. Concus, "Numerical solution of the nonlinear magnetostatic-field equation in two dimensions," *J. Comput. Phys.* **1**, 330 (1967).
- ⁴⁶L. Paterson, "Radial fingering in a Hele-Shaw cell," *J. Fluid Mech.* **113**, 513 (1981).
- ⁴⁷L. V. Kantorovich and G. P. Akilov, *Functional Analysis*, 2nd ed. (Pergamon, New York, 1982).
- ⁴⁸R. S. Dembo, S. C. Eisenstat, and T. Steihaug, "Inexact Newton methods," *SIAM (Soc. Ind. Appl. Math.) J. Numer. Anal.* **19**, 400 (1982).
- ⁴⁹E. Zeidler, *Nonlinear Functional Analysis and its Applications II/B* (Springer-Verlag, New York, 1990).
- ⁵⁰D. Young and D. Kincaid, "The ITPACK package for large sparse linear systems," in *Elliptic Problem Solvers*, edited by M. Schultz (Academic, New York, 1981), p. 163.
- ⁵¹M. Ben Amar, "Exact self-similar shapes in viscous fingering," *Phys. Rev. A* **43**, 5724 (1991).
- ⁵²M. Ben Amar, V. Hakim, M. Mashaal, and Y. Couder, "Self-dilating viscous fingers in wedge-shaped Hele-Shaw cells," *Phys. Fluids A* **3**, 1687 (1991).
- ⁵³Y. Tu, "Saffman-Taylor problem in sector geometry: Solution and selection," *Phys. Rev. A* **44**, 1203 (1991).
- ⁵⁴S. C. Huang and M. E. Glicksman, "Fundamentals of dendritic solidification II: Development of sidebranch structure," *Acta Metall.* **29**, 717 (1981).
- ⁵⁵G. Daccord and J. Nittmann, "Radial viscous fingers and diffusion-limited aggregation: Fractal dimensions and growth sites," *Phys. Rev. Lett.* **56**, 336 (1986).
- ⁵⁶J. Nittmann, G. Daccord, and H. E. Stanley, "When are viscous fingers fractal?" in *Fractals in Physics*, edited by L. Pietronero and E. Tosatti (North-Holland, Amsterdam, 1986).
- ⁵⁷M. Kawaguchi, A. Shibata, K. Shimomoto, and T. Kato, "Effect of geometry and anisotropy of a Hele-Shaw cell on viscous fingering of polymer solutions," *Phys. Rev. E* **58**, 785 (1998).
- ⁵⁸E. Meiburg and G. M. Homsy, "Nonlinear unstable viscous fingers in Hele-Shaw flows. 2. Numerical-simulation," *Phys. Fluids* **31**, 429 (1988).
- ⁵⁹S. K. Sarkar and D. Jasnow, "Viscous fingering in an anisotropic Hele-Shaw cell," *Phys. Rev. A* **39**, 5299 (1989).
- ⁶⁰D. A. Kessler, J. Koplik, and H. Levine, "Pattern selection in fingered growth phenomena," *Adv. Phys.* **37**, 255 (1988).
- ⁶¹M. Kawaguchi, K. Makino, and T. Kato, "Comparison of viscous fingering patterns in polymer and Newtonian solutions," *Physica D* **105**, 121 (1997).
- ⁶²A. J. DeGregoria and L. W. Schwartz, "Finger breakup in Hele-Shaw cells," *Phys. Fluids* **28**, 2313 (1985).
- ⁶³W.-S. Dai and M. J. Shelley, "A numerical study of the effect of surface tension and noise on an expanding Hele-Shaw bubble," *Phys. Fluids A* **5**, 2131 (1993).
- ⁶⁴P. Palfy-Muhoray, R. Ennis, M. J. Shelley, and L. Kondic (in preparation).
- ⁶⁵G. M. Homsy, "Viscous fingering in porous media," *Annu. Rev. Fluid Mech.* **19**, 271 (1987).
- ⁶⁶J. A. Miranda and M. Widom, "Radial fingering in a Hele-Shaw cell: A weakly nonlinear analysis," *Physica D* **120**, 315 (1998).
- ⁶⁷D. Gilbarg and N. S. Trudinger, *Elliptic Partial Differential Equations of Second Order*, 2nd ed. (Springer-Verlag, New York, 1983).